nature neuroscience

Vesicular glutamate release from axons in white matter

Maria Kukley[1], Estibaliz Capetillo-Zarate[2] & Dirk Dietrich[1]

Vesicular release of neurotransmitter is the universal output signal of neurons in the brain. It is generally believed that fast transmitter release is restricted to nerve terminals that contact postsynaptic cells in the gray matter. Here we show in the rat brain that the neurotransmitter glutamate is also released at discrete sites along axons in white matter in the absence of neurons and nerve terminals. The propagation of single action potentials along axons leads to rapid vesicular release of glutamate, which is detected by ionotropic glutamate receptors on local oligodendrocyte precursor cells. Axonal release of glutamate is reliable, involves highly localized calcium microdomain signaling and is strongly calcium cooperative, similar to vesicle fusion at synapses. This axonal transmitter release represents a widespread mechanism for high-fidelity, activity-dependent signaling at the axon-glia interface in white matter.

Throughout the nervous system, the exocytosis of neurotransmitter-filled vesicles at specialized structures called synapses represents the universal signaling mechanism that underlies the transmission of electrical activity from one neuron to another. Fast vesicular transmitter release (<1 ms) requires a complex set of proteins that mediate the calcium-dependent fusion of the vesicular membrane with the presynaptic plasma membrane[1]. A complete set of these proteins is concentrated only at a specialized area of the presynaptic membrane that is directly opposed to the neurotransmitter receptor apparatus of the postsynaptic density[2]. This spatial restriction of transmitter release is a fundamental concept of information processing in the brain, as it enables neurons to signal specifically to their target cells (that is, to neurons that are contacted by synapses) and allows directed signal propagation in neuronal networks.

Recent experimental evidence indicates that sites of synaptic vesicle exocytosis might not always coincide with the postsynaptic density. In the cerebellar cortex, climbing fibers release glutamate from other parts of the presynaptic membrane that do not face the synaptic cleft[3]. Another case of an unusual transmitter release site has been reported at the chick ciliary ganglion, where numerical simulations indicate that release must happen from a wider area of the presynaptic membrane[4] than only the part opposite the postsynaptic density. Although these findings show that the site of transmitter release might vary within a nerve terminal, they are still compatible with the classical view that fast vesicle fusion occurs exclusively at synaptic boutons. Our data show that a similarly specialized exocytotic and endocytotic machinery is also available along axonal compartments.

RESULTS

White matter cells detect axonal glutamate release

To investigate whether rapid neurotransmitter release occurs at parts of the axonal membrane that are far from presynaptic terminals, we tested for quantal transmitter release in white matter regions of the brain. Because white matter primarily contains axons and glia and largely lacks typical postsynaptic targets such as neuronal spines, dendrites and somata, the release of neurotransmitter is not expected in these areas. White matter contains many oligodendrocyte precursor cells (OPCs), which are ideally suited as biological detectors of transmitter release because they express high levels of various neurotransmitter receptors *in vivo* and *in vitro*[5,6]. We prepared slices containing the corpus callosum from juvenile rats (postnatal day (P) 8–16) and selected OPCs for patch-clamp recordings (**Fig. 1**) on the basis of their characteristic expression pattern of voltage-gated ion channels[7] (see Methods). We verified their identity by post-recording immunohistochemistry for the OPC marker NG2[8] (**Fig. 1b**; four out of four cells were positive). At P9, 84% of $NG2^+$ cells in the corpus callosum (229 of 274) were also labeled by O4 (**Fig. 1c**), a marker of late OPCs (which are also called pre-oligodendrocytes[8,9]). We found a similar overlap between NG2 and O4 in the corpus callosum of P9 mice (data not shown).

During patch-clamp recordings of OPCs, we briefly stimulated callosal axons with a second glass pipette. Immediately after the stimulation we recorded fast-rising (rise $time_{20–80\%} = 655 \pm 44$ µs, $n = 8$ cells) and fast-decaying ($\tau_{decay} = 1.9 \pm 0.2$ ms, $n = 8$) inward currents (holding potential, –80 mV) which we termed axo-glial currents (AGCs). AGCs could be recorded in every OPC and depended on the generation of axonal action potentials (**Fig. 1e**) and on voltage-gated calcium channels (**Fig. 1g**). Furthermore, stimulated AGCs showed a characteristic trial-to-trial fluctuation including failures of release (**Fig. 1e–g**). AGCs were reversibly blocked by the AMPA/kainate receptor antagonist 6-cyano-7-nitroquinoxaline-2,3-dione (CNQX, 10 µM; **Fig. 1f**) and reversed at –11 mV (linear fit to average currents, **Fig. 1i**; $n = 6$) as predicted for a mixed Na^+/K^+ conductance mediated by ionotropic glutamate receptors. We did not detect GABA-mediated

[1]Experimental Neurophysiology, Department of Neurosurgery, and [2]Department of Neuropathology, University Clinic Bonn, Sigmund-Freud-Straße 25, 53105, Bonn, Germany. Correspondence should be addressed to D.D. (dirk.dietrich@ukb.uni-bonn.de) or M.K. (maria.kukley@gmx.de).

Received 27 November 2006; accepted 16 January 2007; published online 11 February 2007; doi:10.1038/nn1850

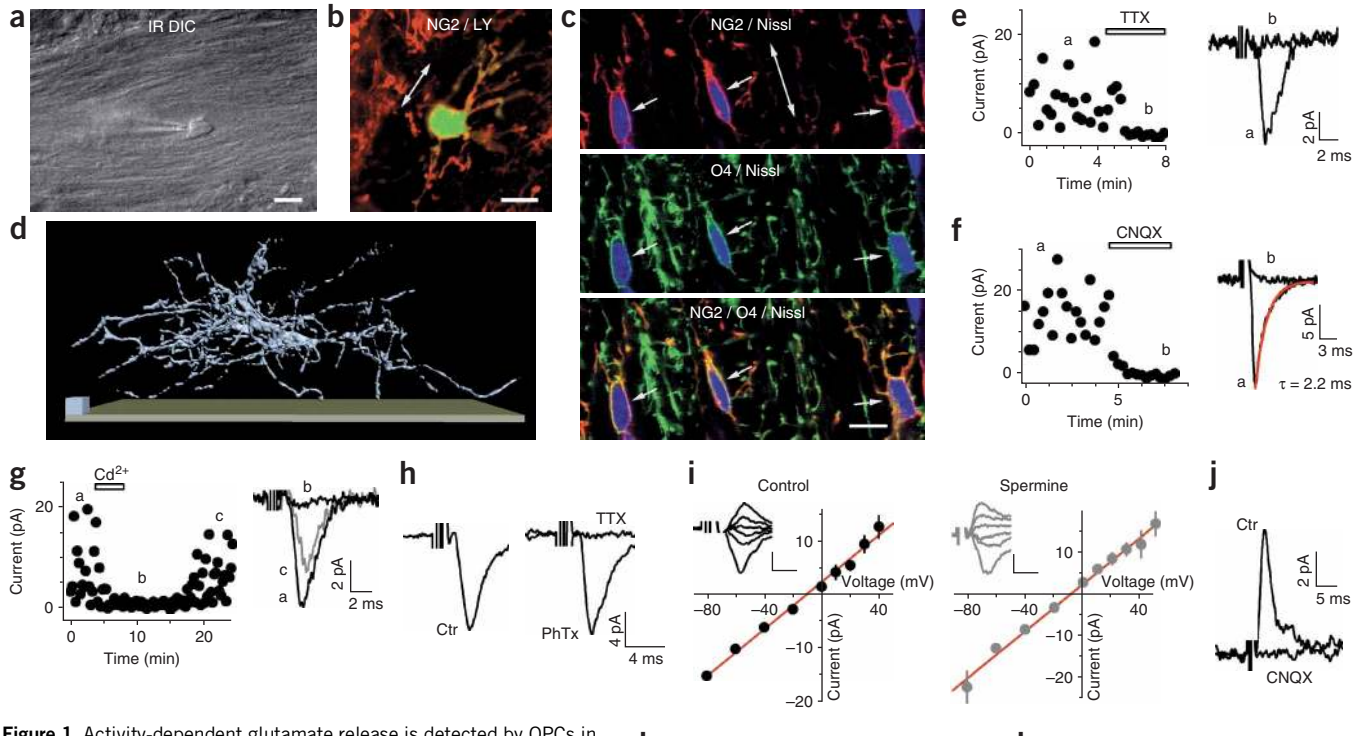

Figure 1 Activity-dependent glutamate release is detected by OPCs in white matter. (**a**) Microphotograph of a corpus callosum slice obtained with infrared differential interference contrast (IR-DIC). Patch pipette approaches OPC from the left. Scale bar, 10 μm. (**b**) Lucifer yellow (LY)-filled OPC, immunoreactive for NG2 (red). Arrows, orientation of callosal axons. Scale bar, 10 μm. (**c**) $NG2^+$ cells in corpus callosum are positive for O4. Top and middle panel, dual-channel images showing Nissl staining (blue), NG2 (red) and O4 (green) labeling, respectively. Bottom panel, triple channel merge illustrating the overlap of the labels (arrows). Double arrow indicates orientation of callosal axons. Scale bar, 10 μm. (**d**) Three-dimensional-isosurface reconstruction of an LY-filled OPC, illustrating the delicate tree of processes. Cube calibrator 3 × 3 × 3 μm^3. (**e**) Left, AGCs are abolished by TTX (0.5 μM, $n = 7$ cells). Right, average currents. Small letters a, b, c on the graph at left indicate the time points for which corresponding example traces are shown at right. (**f**) Left, AGCs are inhibited by CNQX (10 μM, $n = 4$). Right, average currents. (**g**) Left, Cd^{2+} (100 μM, $n = 3$) abolishes AGCs. Right, average currents. (**h**) 15-min bath application of philanthotoxin-433 (PhTx, 10 μM) does not change the amplitude of AGCs (107 ± 11%, $n = 5$). In the same cells, TTX (0.5 μM) abolished AGCs within 5 min. Ctr, control. (**i**) *I-V* relationship without (left) and with (right) 100 μM spermine in internal solution. The curves are scaled to the mean amplitude recorded at –60 mV and represent averages of 4–6 experiments. Inset control: 10 pA, 2 ms. The red line (linear fit) crosses abscissa at –9 mV (spermine). Inset spermine: 4 pA, 2 ms. (**j**) CNQX (10 μM) abolishes AGCs recorded at +40 mV (to 4 ± 2%, $n = 4$). (**k**,**l**) γ-D-Glutamylglycine (DGG, 200 μM) inhibits AGCs in OPCs more strongly (**k**, $n = 6$) than EPSCs in CA1 pyramidal (pyr.) neurons (**l**, $n = 6$).

transmission onto callosal pre-oligodendrocytes, consistent with the fact that most axons traversing the corpus callosum arise from glutamatergic neurons[10].

AMPA receptors that lack the GluR2 subunit are highly permeable to Ca^{2+} ions[11] and show strong inward rectification due to a voltage-dependent block by intracellular polyamines[12]. To test for the presence of GluR2, we applied a specific inhibitor of Ca^{2+}-permeable AMPA/kainate receptors, philantotoxin-433 (ref. 13), and investigated the voltage dependence of AGCs. AGCs were completely insensitive to 10 μM philantotoxin-433 (**Fig. 1h**, in the presence of the NMDA receptor antagonist DL-2-amino-5-phosphonovaleric acid (APV), 50 μM) and did not show signs of inward rectification with ($n = 6$) or without 100 μM of the polyamine spermine (**Fig. 1i**, $n = 4$). We next tested whether NMDA receptors contribute to AGCs. For this we clamped OPCs at positive (+40 mV) potentials to remove the block of NMDA receptors by Mg^{2+}. However, AGCs were still completely blocked by the AMPA/kainate receptor antagonist CNQX (10 μM, $n = 4$; **Fig. 1j**). We conclude that AGCs in white matter OPCs are almost entirely mediated by Ca^{2+}-impermeable AMPA/kainate receptors.

At classical synapses in gray matter, AMPA/kainate receptors are transiently exposed to millimolar concentrations of glutamate[14] owing to the small volume of the synaptic cleft. If a similar geometry underlies AGCs, AMPA/kainate receptors on OPCs should be exposed to comparable glutamate concentrations. We aimed to compare the average glutamate concentration encountered by AMPA/kainate receptors on OPCs to that on hippocampal CA1 pyramidal cells, which also express Ca^{2+}-impermeable AMPA receptors. For this purpose we stimulated a large number of axons and bath applied the low-affinity, rapidly dissociating AMPA/kainate receptor antagonist γ-D-glutamylglycine (γ-DGG, 200 μM; **Fig. 1k**,**l**). Owing to the rapid unbinding kinetics of γ-DGG, the fraction of AMPA/kainate receptors occupied by γ-DGG molecules in the absence of glutamate decreases upon release of glutamate[15]. Therefore, a higher glutamate concentration in the cleft goes along with a lower percentage inhibition of

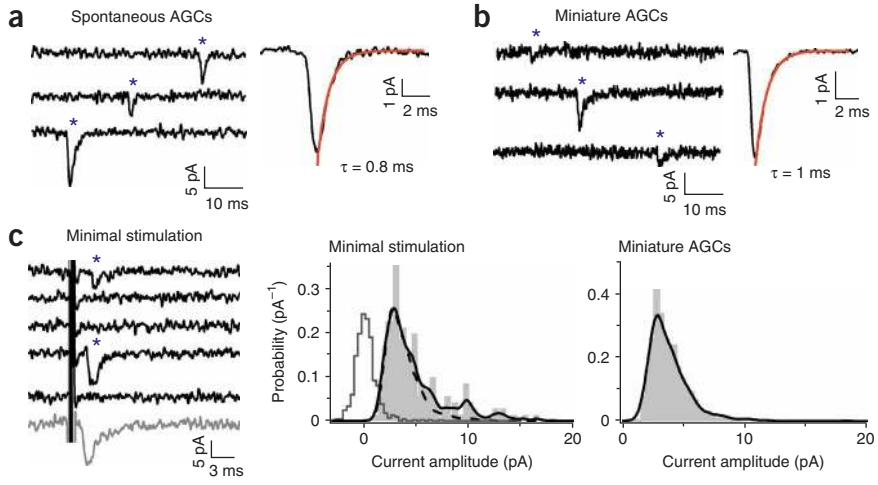

Figure 2 Glutamate release is quantal. (**a**) Fast AGCs (asterisks) occur spontaneously at low frequency ($n = 5$ cells). (**b**) In the presence of TTX and the secretagogue ruthenium red (100 μM), spontaneous quantal events are observed (asterisks, $n = 7$). (**c**) Left, five successive original AGC traces showing responses (asterisks) and failures to minimal stimulation. These failures are failures of release and not of action potential initiation as assessed by a paired-stimulation protocol (ISI 40 ms): the average of responses to the second stimulus that were preceded by a failure was significantly larger than the mean first response ($R_2/R_1 = 1.85 \pm 0.08$, $n = 7$). The gray trace at the bottom is an average of 100 successive trials and is scaled by a factor of 10 for clarity. Middle, amplitude histogram (gray bars) and probability density function (PDF, black line; compare ref. 50) of 201 responses to minimal stimulation (8 OPCs pooled, 100 trials per OPC). Responses were detected and measured with a sliding template algorithm (see Methods). Gray line denotes the amplitude histogram of failures. Dashed line represents the PDF of miniature AGC amplitudes (998 events from 7 cells) scaled to the first peak of the minimal stimulation PDF. Right, amplitude histogram (gray) and PDF (black line) of miniature AGCs.

AMPA/kainate-mediated currents by γ-DGG. γ-DGG depressed AGCs (to 47 ± 3%, $n = 6$) significantly more than it depressed excitatory postsynaptic currents (EPSCs) (to 64 ± 5%, $n = 6$; $P = 0.019$, t-test) recorded in CA1 principal cells (**Fig. 1k**,**l**), indicating that OPCs are exposed to lower concentrations of glutamate than are postsynaptic dendrites in the hippocampus.

AMPA/kainate receptor currents in OPCs are quantal

AGCs also occurred spontaneously, without stimulation, at a frequency of 0.16 ± 0.07 Hz and showed kinetics similar to that of stimulated AGCs (rise time = 330 ± 55 μs, $\tau_{decay} = 1.1 \pm 0.2$ ms, $n = 5$; **Fig. 2a**). Spontaneous AGCs were not observed in the presence of the action potential blocker tetrodotoxin (TTX) and are therefore likely to be due to spontaneous firing of callosal projection neurons in the cortex. In the presence of TTX, miniature AGCs could be provoked by the secretagogue ruthenium red (100 μM; **Fig. 2b**). In the absence of ruthenium red, miniature AGCs were observed too infrequently to be reliably analyzed. In the presence of the drug, they occurred with a frequency of 0.2 ± 0.07 Hz and showed fast kinetics similar to those of stimulated and spontaneous currents (rise time = 191 ± 13 μs, $\tau_{decay} = 1.2 \pm 0.1$ ms, mean amplitude = 4 ± 0.2 pA, $n = 7$). The pharmacological and biophysical properties of AGCs, together with their fast kinetics, indicate that they are mediated by vesicular glutamate release from callosal axons in white matter.

To further investigate the properties of glutamate release from single axons, we performed 'minimal stimulation' experiments, which are designed to stimulate only one presynaptic axon[16] (see also Methods). To confirm that the currents evoked by minimal stimulation originate from a single axon, we compared the mean amplitude of the responses (excluding failures) to the mean amplitude of spontaneously occurring AGCs (for which failures remain undetected). As mentioned above, spontaneous AGCs are due to the firing of callosal projection neurons. As their frequency is low, spontaneous AGCs are almost certainly caused by the activity of single axons and, accordingly, their amplitude should match that obtained by minimal stimulation. The amplitudes of AGCs evoked by minimal stimulation (6.2 ± 0.6 pA, $n = 8$) were not significantly different from the amplitudes of spontaneously occurring AGCs (5.6 ± 0.7 pA, $n = 5$, without TTX, $P = 0.597$).

Using the minimal stimulation protocol, we detected a failure rate of 78 ± 5% ($n = 8$ cells; **Fig. 2c**), implying that the average release probability for a given vesicle, p_{ves}, must be low (< 0.22). Therefore, the mean amplitude (100 trials, including failures) of AGCs evoked by a single axon is small (1.35 ± 0.18 pA, $n = 8$) and yields a mean quantal content, m, of a unitary axon-OPC connection of 1.35 pA/4 pA (mean miniature amplitude) = 0.34 (also see Methods). Although the amplitude distribution obtained by minimal stimulation aligns well with that of miniature AGCs for small currents, it is significantly more skewed towards larger amplitudes (**Fig. 2c**; $D = 0.128$, ($\alpha = 0.01$, Kolmogorov-Smirnov test, 998 and 201 events for miniature and minimal stimulation AGCs, respectively)). Likewise, the amplitude of spontaneous AGCs (caused by single-axon activity) is significantly larger than the amplitude of miniature AGCs (caused by a single vesicle; 5.6 ± 0.7 versus 4 ± 0.2 pA, $P = 0.0439$). These differences might be taken as evidence that a single axon can release more than one vesicle per action potential on a single OPC. Note, however, that this scenario does not imply multivesicular release, as vesicles could be released at different axon-OPC contact sites. Together, the stereotypical amplitude and time course of spontaneous and stimulated responses, the stochastic fluctuation of responses and failures, and the partial overlap of the amplitude distributions of the miniature AGCs and the minimal stimulation currents all support the quantal nature of AGCs. The width of the distributions indicates that pre- and postsynaptic factors produce considerable quantal variability, which is also found at many classical synapses.

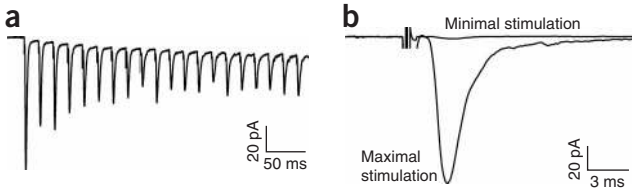

Figure 3 White matter axons contain a pool of releasable vesicles and sustain a high rate of phasic release. (**a**) AGCs evoked by 20 stimuli at 50 Hz (average of 15 sweeps). Towards the end of the train a steady amplitude is reached. (**b**) Maximal stimulation intensity evokes much larger AGCs than minimal stimulation (same cell), indicating that hundreds of axons release transmitter on a single OPC.

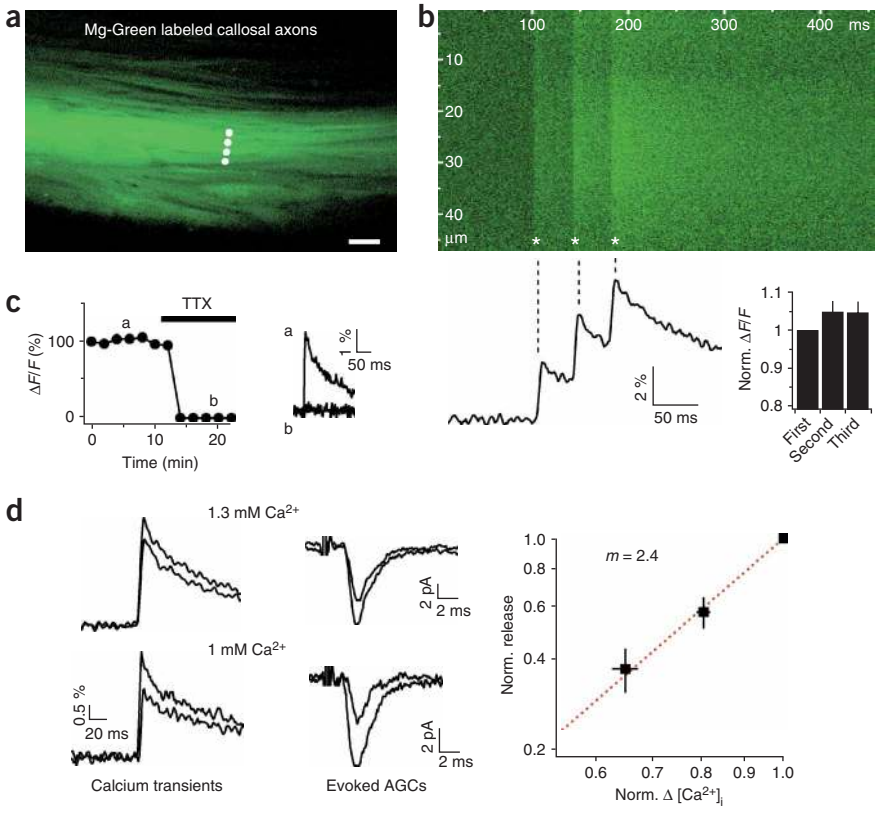

Figure 4 Axonal transmitter release is strongly calcium cooperative. (**a**) Confocal image of a dye-filled axon bundle in the corpus callosum. Dotted line indicates area where repetitive line scans were performed. Scale bar, 40 µm. (**b**) Top, line scan (*y*) against time (*x*) plot of 297 lines scanned at 650 Hz. Asterisks indicate three time points of stimulation at which the fluorescence sharply increases. Bottom, left, trace of fluorescence increases ($\Delta F/F$). A line scan at each time point was averaged to yield one point of the trace. Right, bar graph showing slight facilitation of the three calcium transients ($n = 5$ slices). Norm., normalized. (**c**) Calcium transients are blocked by 1 µM TTX ($n = 4$). (**d**) Left, calcium transients (left column) and AGCs (right column) in control and 1.3 mM extracellular calcium, and in control and 1 mM extracellular calcium. Right, double logarithmic plot of normalized release versus normalized calcium entry as assessed by imaging. Red dashed line represents a fit with a power relationship with an exponent of 2.4.

Reliable high-frequency transmission to OPCs

The components of the presynaptic release machinery that is used to discharge vesicles at synaptic terminals are produced in the soma of the neuron and have to be transported along the axon to synapses[17]. Hence, all of the necessary constituents of a functional release machinery are present in axons. AGCs could therefore represent sporadic release (leak) of vesicles resulting from occasional imperfect targeting of transport vesicles containing presynaptic proteins. In that case, we would expect AGCs to be strongly exhaustible during repetitive activation, and new vesicles to be re-supplied slowly by further axonal transport. To exclude this possibility, we tested how many vesicles are available for release from axons onto OPCs and how quickly vesicles can be replenished during prolonged stimulation. When we applied a 50-Hz train of stimulation to callosal axons, we noticed an initial depression of ACG amplitudes after which they fluctuated around a steady-state value (**Fig. 3a**). We converted the train of AGCs to the corresponding numbers of vesicles released after each stimulation by dividing the charge of the transient current after each stimulation by the quantal charge derived from miniature AGCs recorded in the same cell (for stability of quantal amplitude during the train, see **Supplementary Fig. 1** online). The steady-state quantal content allowed us to estimate that, in response to continuous stimulation, a single axon can sustain a high phasic release rate of 8.3 ± 0.6 vesicles s^{-1} ($n = 7$) onto any neighboring OPC, a value that is well within the known range for neuronal synapses[18]. With some simplifying assumptions, the analysis of the train of AGCs also yields rough estimates of n_{ves}, the number of vesicles that are immediately available for release, and of p_{ves}, the probability that a given vesicle will be released (**Supplementary Fig. 1**). The resulting values are consistent with a classical binomial model of transmitter release from axons (**Supplementary Fig. 2** online). In summary, the substantial rate of persistent phasic release indicates that AGCs are not due to sporadic release of neurotransmitter but instead represent a demanding functional specialization of the axonal membrane.

We next investigated how many axons can release glutamate onto a single OPC. The parallel course of fibers in white matter makes it possible to excite all or at least most of the axons that bypass an individual OPC. The response to maximal stimulation was far larger than that obtained by minimal stimulation (**Fig. 3b**): the transferred charges amounted to 366 ± 18 fC ($n = 5$) and 2.6 fC ($n = 8$, see above), respectively (at –80 mV). The ratio of those two values yields a total of 141 ± 9 axons ($n = 5$) contacting a single OPC. Based on three-dimensional reconstructions of dye-filled OPCs (**Fig. 1c**), we estimate their total surface area and volume to be 1,938 ± 198 µm^2 and 781 ± 94 µm^3, respectively ($n = 9$). Thus, OPCs have at least one functional axon contact for each 14 µm^2 of membrane.

Axonal glutamate release is highly cooperative

Neurotransmitter release at synapses requires a strong elevation of the intracellular free calcium concentration[19]. It is not known whether there is an adequate number of calcium channels in the membrane of axons in white matter to mediate such calcium increases during single action potentials. We performed calcium imaging experiments to directly investigate changes in axonal calcium concentration. We used confocal laser scanning microscopy to visualize axon bundles in the corpus callosum filled with the low-affinity calcium indicator magnesium green (**Fig. 4a**). During electrical stimulation of callosal axons, we repeatedly executed fast-line scans to track changes in the fluorescence of the dye associated with action potentials (**Fig. 4b**). Immediately after stimulation, fluorescence sharply increased and decayed back to baseline with a time constant of 69 ± 8 ms ($n = 5$, **Fig. 4b**). As observed for AGCs, these calcium transients depended on action potential generation (**Fig. 4c**) and were slightly facilitated at an inter-stimulus interval (ISI) of 40 ms (**Fig. 4b**). Thus, voltage-gated calcium channels are clearly present along axon tracts in white matter and mediate similar calcium elevations to those observed in nerve terminals[20].

Calcium induces vesicle fusion at classical synapses with a high cooperativity[21]. High cooperativity is the basic principle that supports

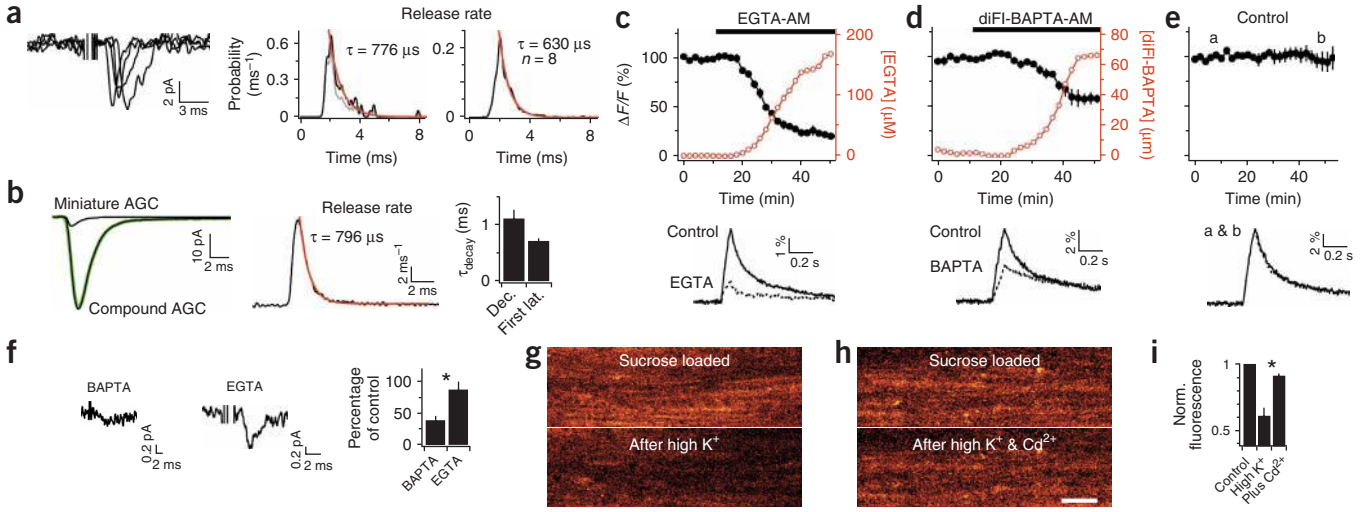

Figure 5 Glutamate release is highly synchronous, mediated by calcium microdomains and involves membrane recycling. (**a**) Time course of release rate as determined by first latency measurements (compare ref. 25). Left, original traces showing variable delay. Middle, PDF (see **Supplementary Methods**) of first latencies ($s(t)$) of same cell (gray). PDF of calculated release rate ($s(t)/(1–S(t))$) (black) ($s(t)$ and $S(t)$ are as defined in ref. 25). Red line, exponential fit to the decay phase of release. Time is given as interval following the onset of stimulation. Right, average of peak aligned release rates from eight cells. (**b**) Time course of release rate as determined by deconvolution (Dec.). Left, superposition of miniature AGC, compound AGC and re-convolution (green) of estimated release rate with miniature AGC. Middle, estimated release rate (quanta per ms) from experiment shown on left. Red line, exponential fit to the decay phase. Right, summary of decay time constants determined with both approaches. First lat., first latency. (**c**–**e**) Time courses of amplitudes of axonal calcium transients evoked by 10 pulses at 100 Hz (black line) during perfusion of EGTA-AM (**c**; $n = 4$, reduction to 21 ± 3%), diFI-BAPTA-AM (**d**; $n = 4$, reduction to 51 ± 5%) and control solution (**e**; $n = 4$, 100 ± 11%). Red curves indicate the intra-axonal chelator concentration reached. Sample traces are shown beneath the time course graphs. (**f**) Only diFI-BAPTA-AM (BAPTA), but not EGTA-AM (EGTA), reduces release probability. Traces represent averages of 100 trials of minimal stimulation after incubation of slices with the calcium chelators. Bar graph summarizes amplitudes as percentage of control incubation ($n = 3$ cells). *, significant difference between current amplitude in BAPTA and EGTA. (**g**) FM1-43 imaging in the corpus callosum. Top, brief exposure to sucrose and FM1-43 (15 µM) leads to FM1-43 uptake by callosal fibers. Bottom, 45 mM K^+ induces de-staining of corpus callosum. (**h**) As in **g** but de-staining by K^+ is prevented by 100 µM Cd^{2+} and low external calcium. Scale bar, 50 µm. (**i**) Summary bar graph of calcium-dependent de-staining of corpus callosum, showing the remaining fluorescence measured after high K^+ perfusion in the absence and in the presence of Cd^{2+} ($n = 4$ slices each). *, significant difference between normalized fluorescence in high K^+ alone and high K^+ and Cd^{2+}).

the high fidelity of neuronal communication, by allowing different forms of synaptic plasticity and the effective modulation of transmission by various neurotransmitter receptors[21]. We determined the calcium cooperativity of axonal glutamate release by combining the results of axonal calcium imaging with patch-clamp recordings of AGCs. We reduced the extracellular calcium concentration to 1.3 and 1 mM (balanced with Mg^{2+}) in order to modulate the single channel calcium currents (by reducing the occupancy of the channel pore[22]). Changes in free calcium concentration at the calcium sensor and changes in free global calcium concentration ('bulk calcium', as assessed by our confocal calcium imaging) are both proportional to changes in the single-channel calcium current[23]. Therefore, the reduction in axonal calcium transients that is induced by perfusing the cells with low extracellular calcium can be used as a measure of the reduction in the short-lived calcium increases that are caused by an action potential at the calcium sensor. Calcium transients were only slightly reduced, to 81 ± 2% ($n = 4$) and 65 ± 2% ($n = 4$), by perfusion of 1.3 and 1 mM calcium, respectively (**Fig. 4d**). By contrast, AGCs (transferred charges) were substantially inhibited to 57 ± 7% ($n = 4$) and 37 ± 6% ($n = 4$) by the same calcium concentrations (**Fig. 4d**). A double logarithmic plot of normalized release against the normalized calcium increases after an action potential revealed that axonal glutamate release is highly cooperative and obeys a power relationship with calcium that has an exponent of 2.4 (**Fig. 4d**). This value is very close to the estimates obtained for neuronal synapses, and indicates that similar calcium sensors, binding at least three calcium ions, might be involved in synaptic and axonal glutamate release[24].

Synchronous glutamate release triggered by Ca^{2+} microdomains

After an action potential arrives at a presynaptic terminal, transmitter is released only for a brief time (a few milliseconds). This high synchrony of vesicle release is necessary to transmit high-frequency signals and to improve the temporal discrimination of responses in the postsynaptic neuron. We have investigated the kinetics of axonal transmitter release in two ways. The first approach is based on measurements of the first latencies of quantal responses[25] (**Fig. 5a**). For this approach we used low stimulation intensities that yield a quantal content < 0.8 (≤ 3 axons). Second, we obtained the time-course of transmitter release by deconvolution of a compound AGC with a quantal response (average miniature AGC) recorded in the same cell (**Fig. 5b**; see ref. 26 and Methods). Both procedures show that axonal transmitter release after a single action potential is highly synchronized, steeply increases to a sharp peak and then rapidly decays back to baseline ($\tau_{decay} = 706 \pm 56$ µs, $n = 8$, and $\tau_{decay} = 1.1 \pm 0.2$ ms, $n = 6$, respectively). This fast decay of the release rate implies that the underlying calcium signal must also be very short-lived[27]. As such rapid calcium signals arise only in the immediate vicinity of calcium channels[28], within so-called calcium microdomains[29], the kinetics of release support the idea that axonal vesicles and axonal voltage-gated calcium channels are closely associated.

If Ca^{2+} microdomains are involved in axonal transmitter release, it should be differentially affected by the calcium chelators BAPTA and EGTA. At similar concentrations, BAPTA is much more effective than EGTA at reducing the free calcium concentration close to the calcium source, in a microdomain, because it captures calcium ions around

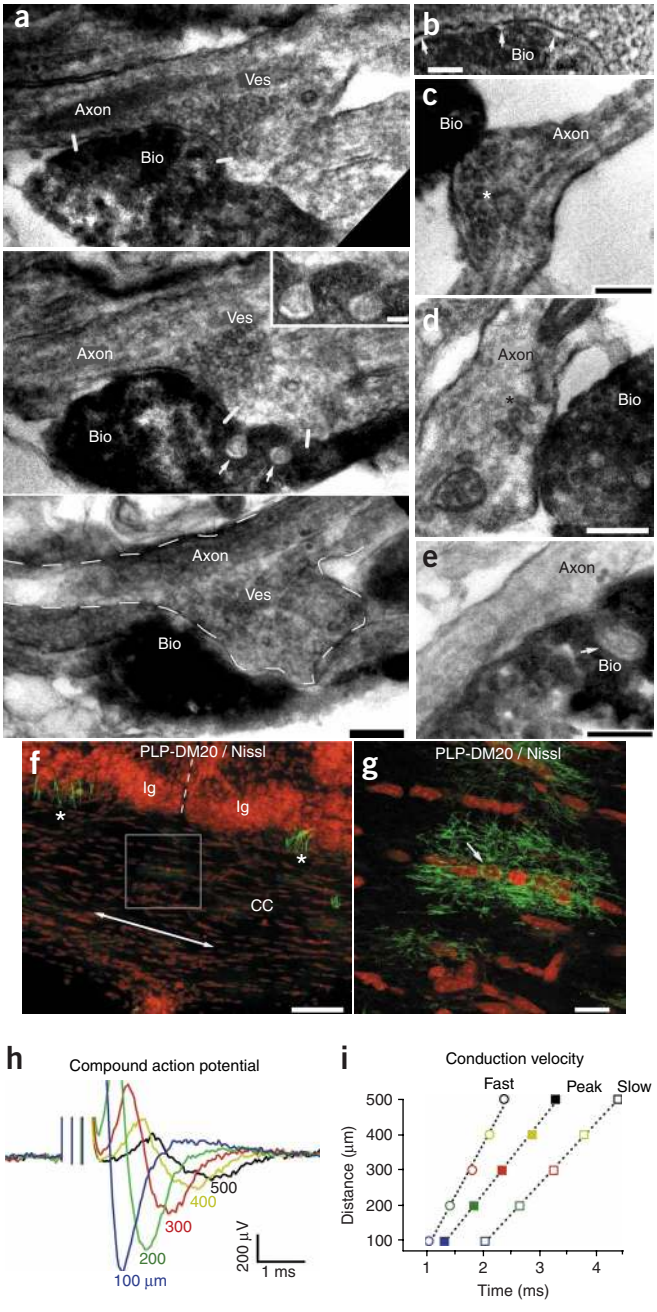

Figure 6 Unmyelinated axons contain synapse-like vesicles at contact sites with OPCs. (**a**) Electron microscopic analysis of the relationship of biocytin-filled processes (Bio) of OPCs with neighboring axons. Three serial sections of a contact site are shown. Scale bar, 200 nm. The axon forms a small varicosity containing many vesicles (Ves). Note that small protrusions of the axonal membrane form glial invaginations (arrows in middle section). Inset in middle panel shows magnified view of invaginations between white bars (inset scale bar, 50 nm). In the bottom panel a dashed line indicates the outline of the axon. (**b**) Magnification of the area in top panel of **a** that is indicated by two white bars. The cleft shows an irregular width and apparently lacks an extracellular matrix (arrows). Some vesicles appear to be 'docked' on the axonal membrane. Scale bar, 100 nm. (**c**) Another contact site where the axon widens only minimally to accommodate the vesicles (asterisk). Scale bar, 200 nm. (**d**) As in **c** but with a smaller number of vesicles (asterisk). Scale bar, 200 nm. (**e**) Another invagination of axonal membrane into the OPC membrane. Note the constant spacing between axonal and OPC membranes (arrow). Scale bar, 200 nm. (**f**) PLP/DM20 (green) and Nissl (red) staining of P10 corpus callosum (CC). Callosal axons (direction indicated by double arrow) are PLP-negative. PLP staining of myelin is observed only in axons (asterisks) leaving the Indusium griseum (Ig). Note weakly stained large cells in corpus callosum. The boxed cell is magnified in **g**. Dashed line, midline of the brain. Scale bar, 100 µm. (**g**) Magnification of box in **f**. Maximum merge of three neighboring confocal scans ($\Delta z \sim 1$ µm). The arrow points to a typical pre-myelinating oligodendrocyte expressing DM20 on its entire surface. Scale bar, 20 µm. (**h**) Stimulating electrode was fixed and action potentials were recorded extracellularly at different distances from the stimulation site. Owing to slightly different conduction velocities, the signal broadens and decreases in amplitude with distance. (**i**) Even the fastest conduction velocity is <1 m s^{-1}, well in the range of that of unmyelinated fibers. For the curve labeled 'peak', the time of the action potential peak was plotted against distance. To estimate the fastest and slowest velocities, the two time points at which the action potentials reach 10% of their maximal amplitudes were plotted against distance.

100 times faster than EGTA[30]. We used the membrane-permeable derivates EGTA-AM and 5,5′-difluoro BAPTA-AM (diFl-BAPTA-AM) to load callosal axons with calcium chelators. We monitored the loading efficacy by axonal calcium imaging (**Fig. 5c–e**) while continuously perfusing the chelators (see Methods). In these experiments, we stimulated axons with a brief train of ten pulses at 100 Hz to allow the dissipation of any diffusional calcium gradients and to obtain a robust response that could be recorded for >50 min (**Fig. 5e**). The amplitudes of the calcium transients that were evoked by this stimulation slowly decreased during perfusion of the calcium chelators. On the basis of the single-compartment model of calcium buffering[23], we can use the reduction in the amplitudes of calcium transients to estimate the intracellular chelator concentration, so long as we can estimate the endogenous buffer content and indicator dye concentration. We used values previously established for unmyelinated axons in the cerebellum[31] (see Methods) and estimated that the intra-axonal concentrations of EGTA and diFl-BAPTA-AM were >170 µM and ~65 µM, respectively (**Fig. 5c–e**). We found that loading axons with BAPTA-AM was unreliable (sometimes only a few micromolar accumulated; $n = 8$, data not shown). Therefore, we used diFl-BAPTA-AM, a derivative of BAPTA that has similar rapid binding kinetics. Note that the EGTA concentration is probably underestimated because the increase in free calcium might have partially saturated this high-affinity calcium chelator (K_D = 180 nM compared with 635 nM for diFl-BAPTA). Next, we incubated slices under similar conditions with the chelators (and in control solution) to investigate the effect of chelation on axonal release probability. We performed minimal stimulation experiments and compared the average response of 100 successive trials between groups (**Fig. 5f**). As we would expect if calcium microdomains trigger transmitter release, only diFl-BAPTA-AM (n = 4), but not EGTA, substantially reduced transmitter release to 38 ± 5% (EGTA to 87 ± 12%, n = 3) of the control group (**Fig. 5f** right panel; EGTA versus BAPTA $P = 0.016$, t-test). The differential effect of the two buffers was quantitatively similar when analyzing the failure rate: control group, 85 ± 2% (15% responses); EGTA, 88 ± 2% (12% responses); BAPTA, 95 ± 1% (5% responses). This indicates that the quantal amplitude was unaffected by BAPTA.

Taking advantage of both the relationship between calcium and release (as shown in **Fig. 4d**) and an approximation of the buffering effect of diFl-BAPTA-AM (**Fig. 5d**), we can make a rough estimate of the spatial extent of the microdomains involved. Taking into account experimental errors, we estimate that the distance between the calcium source (voltage-gated calcium channels) and the calcium sensor (which

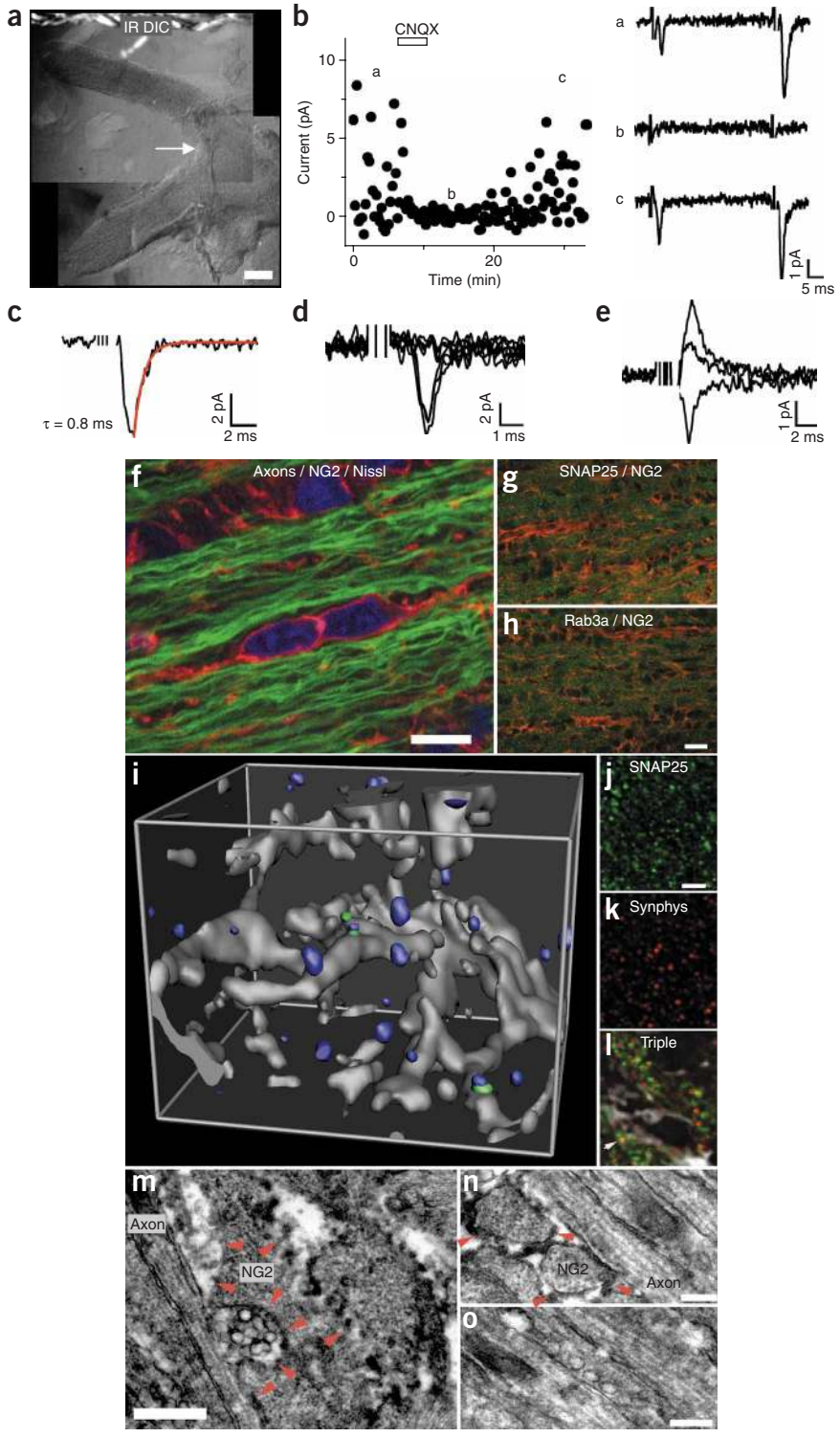

Figure 7 Axonal transmitter release might occur at arbitrary release sites along white matter axons. (**a**) IR-DIC image of combined optic nerve and chiasm (arrow) slice preparation. Scale bar, 200 μm. (**b**) Time-course and sample traces of AGCs evoked by paired-pulse stimulation of RGC axons (ISI, 40 ms). AGCs are blocked by 10 μM CNQX (holding potential –80 mV, $n = 6$ cells). (**c**) Average AGC recorded in OPC in optic nerve slice preparation. (**d**) Superimposed successive trials of AGCs showing responses and failures. (**e**) Reversal of AGCs in optic nerve OPCs around the predicted equilibrium potential for ionotropic glutamate receptors (currents recorded at –80, 0 and +30 mV). (**f**) Triple channel confocal image showing the tight spatial relationship between OPCs in optic nerve (labeled by NG2 antibodies; red) and RGC axons (biocytin filled; green). Nuclei are stained blue (Nissl stain). Scale bar, 10 μm. (**g**) Dual-channel image showing many SNAP25 puncta (green) between rows of $NG2^+$ cells (red). Scale bar, 20 μm. (**h**) As in **g**, but stained for Rab3a rather than SNAP25. Scale bar, 20 μm. (**i**) Triple channel isosurface reconstruction. Gray, NG2 staining. Blue, colocalization of synaptophysin and SNAP25. Green, contact sites of $NG2^+$ membranes with colocalized synaptophysin and SNAP25. Most synaptophysin/SNAP25 spots do not contact OPCs. Box size $15.5 \times 13.7 \times 13.3$ μm^3 scanned with $74 \times 86 \times 75$ voxels. (**j**,**k**) *z*-maximum projections of the image stacks after deconvolution as used for reconstruction in **i**. There are many more SNAP25 and synaptophysin (Synphys) spots than blue spots on the left because fewer than 10% of spots co-localize. Also, the same (*x*,*y*) position of two spots in these panels does not necessarily reflect co-localization as the spots may be from different *z* planes. Scale bar, 3 μm. (**l**) Illustrates *x*,*y* plane no. 67, which contains the green spot in the lower right corner of the three-dimensional reconstruction. Arrows shows the pixel overlap of the three channels in this plane. SNAP25, green; synaptophysin, red; NG2, gray. (**m**) Pre-embedding immuno-electron microscopy for NG2 in P8 optic nerves. Red arrowheads, drop-like diamino-benzidine (DAB) product of NG2 labeling. $NG2^+$ process contacts an axon containing many vesicles. Scale bar, 500 nm. (**n**) As in **m** but no vesicles are seen at axon-$NG2^+$ contacts. Scale bar, 200 nm. (**o**) As in **n**, but vesicles in axon do not face an $NG2^+$ membrane. Scale bar, 200 nm.

mediates transmitter release) must be smaller than 100 nm (**Supplementary Fig. 3** online).

Axonal glutamate release involves endo- and exocytosis

Our data indicate that axons can rapidly replenish vesicles during a train of action potentials. If exocytosis underlies AGCs, then during replenishment endocytosis must compensate for release. Vesicular endocytosis and exocytosis can be visualized in intact brain slices using the styryl fluorescent dye FM1-43 (ref. 32) (see Methods). To test for vesicular membrane recycling, we induced strong exocytosis by briefly exposing slices containing the corpus callosum to artificial cerebrospinal fluid (ACSF) supplemented with hyperosmolaric sucrose and FM1-43 (ref. 33). After thorough washing in dye-free solution and quenching of extracellular FM1-43 with sulforhodamine-101, we viewed the corpus callosum with a confocal laser microscope. Under these conditions, we observed fluorescently labeled longitudinal stripes, which might represent axon fascicles, that contained internalized vesicles containing FM1-43 (**Fig. 5g**,**h**). Inducing neuronal activity by perfusing the slices with a high concentration of K^+ for 40 s led to a significant decrease in fluorescence ($P = 0.016$, $n = 4$, *t*-test;

Fig. 5g), indicating that exocytosis had occurred and caused the release of FM1-43, which was then washed away and quenched. The de-staining of putative axon fascicles was prevented if calcium entry was blocked pharmacologically (**Fig. 5h,i**; $P = 0.005$, *t*-test). Thus, the activity-dependent staining and de-staining of the corpus callosum with FM1-43 supports the idea that callosal axons are capable of highly dynamic exo-endocytotic recycling of glutamate-filled vesicles.

Unmyelinated axons contain synaptic-like vesicles

To obtain ultrastructural evidence for vesicles at axon-OPC interfaces, we filled five electrophysiologically identified OPCs (at P15–P16) with biocytin during whole-cell recordings and processed them for electron microscopy. At contact sites between unmyelinated axons and thin OPC processes, we found accumulations of small vesicles close to the axonal membrane (**Fig. 6a–d**). In single ultra-thin sections, we found between a few (**Fig. 6d**) and ~40 vesicles (**Fig. 6a**) on the axonal side of these contact sites. The vesicles accumulated in minimal to small axonal varicosities (<400 nm). The cleft between the cells appeared clear and had an irregular width (**Fig. 6b**). Our ultrastructural analysis also revealed a morphological interaction between OPCs and axons, which consists of small protrusions of axonal membranes into the glial compartment (**Fig. 6a,e**). The function of these glial invaginations is unclear, but they bear some similarities to so-called synaptic spinules, which have been suggested to serve transcellular endocytosis[34]. Note that, in agreement with earlier ultrastructural studies[35,36], we found that very few callosal axons were ensheathed (<2%) at this age, and most of these axons had only one or two layers of uncompacted myelin.

To rule out the involvement of myelinated axons in AGCs, we performed immunostaining for proteolipid protein (PLP), one of the main constituents of myelin, and determined the conduction velocity of axons that we stimulated to evoke AGCs. Consistent with earlier studies (compare **Fig. 2** in ref. 37), we did not detect PLP-containing myelin along callosal axons at this developmental stage (P10; **Fig. 6f,g**). Furthermore, action potentials (recorded in the presence of 2 mM kynurenic acid in P8 rats) propagated even in the fastest fibers at a slow speed of less than 0.3 m s^{-1} (**Fig. 6h,i**). Together, the morphological and functional evidence indicates that glutamate is released from unmyelinated axons.

Glutamate release is widespread in white matter

Although the corpus callosum is a white matter structure, it contains some scattered interstitial neurons[38], raising the question of whether glutamate release is a signal from bypassing axons or whether it might represent a specific local projection from these interstitial neurons. Unlike the corpus callosum, optic nerves do not contain neurons or neuronal progenitors at any time during development. Therefore we recorded from OPCs in optic nerve slices (**Fig. 7a**) and stimulated retinal ganglion cell (RGC) axons. As would be expected if AGCs are a widespread signal at the axon-OPC interface, we observed identical inward currents as in the corpus callosum, which also appeared in a quantal fashion and showed the same pharmacological and biophysical properties (**Fig. 7b–e**).

At the early developmental stage we are investigating, the production of OPCs in the corpus callosum and optic nerve is still ongoing[39]. Considering that quantal synaptic currents are not observed in newborn neurons until their second week[40,41], it seems surprising that axons in white matter can rapidly recognize newborn OPCs and establish functional release sites with these immature glial cells much more quickly. We therefore investigated whether axons release transmitter not only at contact sites with OPCs but also at arbitrary sites. In this case, some released glutamate would remain undetected while other glutamate bound to glutamate receptors on OPC membranes, which are sufficiently close to the site of release. OPCs are well suited for detecting glutamate release, as they are embedded in axon bundles and extend multiple fine processes between neighboring nerve fibers (**Fig. 7f**). To localize vesicle release sites we stained optic nerves for various presynaptic fusion proteins. We found punctate staining for SNAP25, Rab3, synaptophysin (**Fig. 7**), synaptotagmin-1, synaptobrevin and syntaxin (data not shown) located within the axon bundles between the fascicles of $NG2^+$ OPCs. However, most of this staining could be attributed to axonal transport of presynaptic proteins to the nerve terminals of retinal ganglion cells. To identify putative assembled presynaptic fusion proteins, we performed double immunostaining for synaptophysin and SNAP25. These two proteins are not expected to be transported together because SNAP25 is targeted to the plasma membrane and synaptophysin to the vesicular membrane[42]. A fraction of SNAP25 and synaptophysin punctae colocalized (**Fig. 7i**, blue), which might represent vesicle release sites. In a third channel, we stained OPC membranes with anti-NG2 antibodies. As shown in **Fig. 7i**, $SNAP25^+$ and $synaptophysin^+$ punctae appear to be largely randomly distributed and only a small portion of them are in contact with OPC membranes (**Fig. 7i**, green; also see **Fig. 7j–l**).

We further analyzed the ultrastructure of OPC-axon contacts in optic nerves by electron microscopy and pre-embedding immunohistochemistry for NG2. As observed in the corpus callosum, small clusters of vesicles opposed to NG2-labeled membranes are found along axons (**Fig. 7m**). However, vesicles are not found at every contact site (**Fig. 7n**) and not every putative vesicle release site is opposed to $NG2^+$ membranes (**Fig. 7o**).

DISCUSSION

We have shown that fast vesicular neurotransmitter release is not restricted to nerve terminals in the gray matter and is therefore not only the basis of signal propagation in neural circuits. Our data indicate that a separate, similarly specialized exocytotic and endocytotic machinery is also available along axonal compartments. Glutamate release from axons in the white matter has long been postulated but the underlying mechanism has remained controversial[43,44]. Under certain conditions, axons might also release glutamate through reverse uptake, but as vesicular release is triggered with each propagating action potential it is likely that the predominant mode is by vesicular means as shown here.

Although axonal transmitter release is functionally nearly indistinguishable from neurotransmitter release at classical synapses, there are certain differences which might indicate that axonal release is not intended for signaling to a specific postsynaptic cell. These differences include the following: (i) the intercellular cleft lacks a matrix and is relatively wide and irregular (**Fig. 6**), (ii) OPCs sense lower glutamate concentrations than do postsynaptic neurons (**Fig. 1k,l**), (iii) presynaptic fusion proteins colocalize independent of NG2 labeling (**Fig. 7i**) and (iv) axonal vesicles are found in the absence of NG2 membranes (**Fig. 7o**). Therefore, we suggest that axons release transmitter at discrete but arbitrary sites along their surface and not necessarily directly onto OPC membranes. It is possible that OPCs use a concentration gradient of glutamate toward these arbitrary release sites to detect axons. It should also be pointed out that axonal glutamate release might represent a significant metabolic burden: for certain neurons with extended axon lengths, such as interhemispheric projection neurons, the amount of transmitter released along axons should be much greater than the amount of transmitter released from their classical nerve terminals.

We found axonal transmitter release in both the corpus callosum and the optic nerve. Therefore, it seems likely that axonal transmitter release represents a universal signal at the early axon-OPC interface throughout white matter. In contrast to the release of other substances, such as those involved in purinergic signaling[45], the vesicular release of glutamate is ideally suited to guide the development of glial cells in an activity-dependent manner[46,47]: Because of its high spatial (AMPA receptors have a low glutamate affinity) and temporal resolution (AGCs are extremely fast), glutamate release could be used by OPCs to locate axons and to distinguish them from other tubular structures in the neuropil. On the other hand, under pathological conditions the widespread release of glutamate along axon tracts might be harmful: axonal transmitter release is likely to contribute to the ability of NMDA receptors to mediate ischemic damage of mature oligodendrocytes[48]. Therefore, drugs that modulate transmitter release in white matter might be promising therapeutic targets.

Axonal transmitter release might also challenge the concept of exclusively directed signal spread in neuronal networks of the CNS. As the axons in white matter are simply elongations of axons in gray matter, it seems likely that extrasynaptic transmitter release also occurs along intracortical axons and that this activates neurons that are not synaptically connected. The resulting spread of neuronal signals would strongly increase the apparent connectivity of neural circuits and could have a significant impact on information processing in the brain.

METHODS

For a detailed description of Methods please refer to **Supplementary Methods** online.

Corpus callosum slice preparation. Frontal slices (300 μm) were prepared from 8–16-day-old rats, placed in an interface chamber and maintained in ACSF containing (in mM): NaCl 124, KCl 3, NaH_2PO_4 1.25, $MgSO_4$ 2, $CaCl_2$ 2, $NaHCO_3$ 26, glucose 10 and with pH 7.4, osmolality 300 mOsm kg^{-1}, gassed with a 95% O_2 and 5% CO_2 mixture. Individual slices were transferred to a submerged recording chamber mounted on the stage of an upright microscope (Nikon E600FN), and continuously superfused (2 ml min^{-1}) with ACSF. Animals were kept and treated in accordance with national and institutional guidelines. Optic nerves from 3–8-day-old rat pups were isolated, embedded into 5% agar and cooled to 4 °C, and 100–150-μm-thick longitudinal slices were prepared on a vibratome.

Cell identification. As an additional criterion we verified that the amplitudes of voltage-activated currents were consistent with those typically found in white matter OPCs[7,49]: peak amplitude of sodium current at +10 mV, $I_{Na(+10mV)} = 294 \pm 36$ pA; amplitude of transient A-current at +10 mV, $I_{A(+10mV)} = 915 \pm 44$ pA; amplitude of steady state potassium current at +10 mV, $I_{SS(+10mV)} = 386 \pm 22$ pA. All values were determined from leak-subtracted current traces. The typical current pattern is shown in **Supplementary Figure 4** online.

Recording of AGCs with ETGA-AM and BAPTA-AM. Slices were incubated for 1 h in ACSF containing 100 μM diFl-BAPTA-AM or 100 μM EGTA-AM, 175 μM probenecid, 70 μM 2-hydroxypropyl-β-cyclodextrin and 0.1% DMSO and pluronic acid. In the recording chamber we perfused slices with ACSF containing 1 μM diFl-BAPTA-AM or 1 μM EGTA-AM, 1 mM probenecid and 70 μM 2-hydroxypropyl-β-cyclodextrin. Control slices were incubated in the same solution, but containing only 0.1% DMSO and pluronic acid. The mean current amplitude over 100 trials was calculated for each cell and averaged within each group. The group averages with BAPTA and EGTA were then normalized on the group average of the control group and expressed as a percentage.

Calcium imaging. Callosal axons were loaded with the low-affinity Ca^{2+} indicator magnesium green. The amplitude of the Ca^{2+} fluorescence signal was measured as the ratio of the difference between the peak fluorescence (ΔF) and the resting fluorescence (F). During imaging we bath applied 100 μM of the calcium chelators in the presence of 175 μM probenecid, 70 μM 2-hydroxypropyl-β-cyclodextrin and 0.1% DMSO and pluronic acid.

FM1-43 imaging. Corpus callosum slices were incubated for 10 min in ACSF plus 15 μM FM1-43. Next, slices were exposed for 20 s to ACSF plus 800 mM sucrose and returned for 2 min to ACSF plus FM1-43. After that, slices were washed for 15 min in FM1-43-free ACSF containing 100 μM sulforhodamin-101 and scanned. To unload FM1-43, we perfused slices for 40 s with ACSF containing 45 mM K^+ or ACSF containing 45 mM K^+, 100 μM $CdCl_2$ and 0.5 mM $CaCl_2$ (substituted equimolarly by $MgCl_2$). Subsequently, we perfused with ACSF for 10 min and then acquired the second scan.

Pre-embedding immunohistochemistry for NG2. P8 rats were anesthetized and transcardially perfused. 50-μm optic nerve sections were prepared on a vibratome and stained for NG2, without Triton-X.

Electron microscopy. 50-μm sections (biocytin-filled OPCs and NG2-stained optic nerves) were post-fixed with 1% osmium tetraoxide containing 0.8% potassium ferrocyanide for 120 min, and embedded in epoxy resin. Ultra-thin sections were visualized with a Philips CM10 transmission electron microscope.

Note: Supplementary information is available on the Nature Neuroscience website.

ACKNOWLEDGMENTS

We thank S. Schoch for discussions and comments on the manuscript and for sharing reagents; D. Thal and J. Bedorf for help with electron microscopy; R. Buettner and D. Thal for sharing equipment; B. Stallcup and B. Zalc for providing antibodies. This study was supported by Deutsche Forschungsgemeinschaft (SFB TR3, DI 853/2) and University Clinic Bonn grants (BONFOR). We thank P. Stausberg and K. Neitzert for technical assistance.

AUTHOR CONTRIBUTIONS

M.K. performed patch-clamp recordings; E.C.-Z. and D.D. performed and designed electron microscopy investigations; and D.D. carried out Ca^{2+}- and FM1-43 imaging experiments, extracellular recordings, immunohistochemistry and three-dimensional reconstructions. D.D. and M.K. designed experiments, analyzed data and prepared figures. D.D., M.K. and E.C.-Z. wrote the manuscript. D.D. provided financial support.

COMPETING INTERESTS STATEMENT

The authors declare that they have no competing financial interests.

Published online at http://www.nature.com/natureneuroscience
Reprints and permissions information is available online at http://npg.nature.com/reprintsandpermissions

1. Jahn, R., Lang, T. & Sudhof, T.C. Membrane fusion. *Cell* **112**, 519–533 (2003).
2. Rosenmund, C., Rettig, J. & Brose, N. Molecular mechanisms of active zone function. *Curr. Opin. Neurobiol.* **13**, 509–519 (2003).
3. Matsui, K. & Jahr, C.E. Ectopic release of synaptic vesicles. *Neuron* **40**, 1173–1183 (2003).
4. Coggan, J.S. *et al.* Evidence for ectopic neurotransmission at a neuronal synapse. *Science* **309**, 446–451 (2005).
5. Barres, B.A., Chun, L.L. & Corey, D.P. Ion channels in vertebrate glia. *Annu. Rev. Neurosci.* **13**, 441–474 (1990).
6. Steinhauser, C. & Gallo, V. News on glutamate receptors in glial cells. *Trends Neurosci.* **19**, 339–345 (1996).
7. Berger, T., Schnitzer, J. & Kettenmann, H. Developmental changes in the membrane current pattern, K^+ buffer capacity, and morphology of glial cells in the corpus callosum slice. *J. Neurosci.* **11**, 3008–3024 (1991).
8. Baumann, N. & Pham-Dinh, D. Biology of oligodendrocyte and myelin in the mammalian central nervous system. *Physiol. Rev.* **81**, 871–927 (2001).
9. Sommer, I. & Schachner, M. Monoclonal antibodies (O1 to O4) to oligodendrocyte cell surfaces: an immunocytological study in the central nervous system. *Dev. Biol.* **83**, 311–327 (1981).
10. Jacobson, S. & Trojanowski, J.Q. The cells of origin of the corpus callosum in rat, cat and rhesus monkey. *Brain Res.* **74**, 149–155 (1974).
11. Hume, R.I., Dingledine, R. & Heinemann, S.F. Identification of a site in glutamate receptor subunits that controls calcium permeability. *Science* **253**, 1028–1031 (1991).
12. Bowie, D. & Mayer, M.L. Inward rectification of both AMPA and kainate subtype glutamate receptors generated by polyamine-mediated ion channel block. *Neuron* **15**, 453–462 (1995).
13. Washburn, M.S. & Dingledine, R. Block of α-amino-3-hydroxy-5-methyl-4-isoxazolepropionic acid (AMPA) receptors by polyamines and polyamine toxins. *J. Pharmacol. Exp. Ther.* **278**, 669–678 (1996).

14. Clements, J.D. Transmitter timecourse in the synaptic cleft: its role in central synaptic function. *Trends Neurosci.* **19**, 163–171 (1996).
15. Liu, G., Choi, S. & Tsien, R.W. Variability of neurotransmitter concentration and nonsaturation of postsynaptic AMPA receptors at synapses in hippocampal cultures and slices. *Neuron* **22**, 395–409 (1999).
16. Raastad, M., Storm, J.F. & Andersen, P. Putative single quantum and single fibre excitatory postsynaptic currents show similar amplitude range and variability in rat hippocampal slices. *Eur. J. Neurosci.* **4**, 113–117 (1992).
17. Garner, C.C., Zhai, R.G., Gundelfinger, E.D. & Ziv, N.E. Molecular mechanisms of CNS synaptogenesis. *Trends Neurosci.* **25**, 243–250 (2002).
18. Taschenberger, H., Scheuss, V. & Neher, E. Release kinetics, quantal parameters and their modulation during short-term depression at a developing synapse in the rat CNS. *J. Physiol. (Lond.)* **568**, 513–537 (2005).
19. Augustine, G.J. How does calcium trigger neurotransmitter release? *Curr. Opin. Neurobiol.* **11**, 320–326 (2001).
20. Dietrich, D. *et al.* Functional specialization of presynaptic Cav2.3 Ca^{2+} channels. *Neuron* **39**, 483–496 (2003).
21. Schneggenburger, R. & Neher, E. Presynaptic calcium and control of vesicle fusion. *Curr. Opin. Neurobiol.* **15**, 266–274 (2005).
22. Hille, B. *Ionic Channels of Excitable Membranes* (Sinauer, Sunderland, Massachusetts, USA, 1992).
23. Neher, E. Usefulness and limitations of linear approximations to the understanding of Ca^{++} signals. *Cell Calcium* **24**, 345–357 (1998).
24. Mintz, I.M., Sabatini, B.L. & Regehr, W.G. Calcium control of transmitter release at a cerebellar synapse. *Neuron* **15**, 675–688 (1995).
25. Barrett, E.F. & Stevens, C.F. The kinetics of transmitter release at the frog neuromuscular junction. *J. Physiol. (Lond.)* **227**, 691–708 (1972).
26. Van der Kloot, W. Estimating the timing of quantal releases during end-plate currents at the frog neuromuscular junction. *J. Physiol. (Lond.)* **402**, 595–603 (1988).
27. Meinrenken, C.J., Borst, J.G. & Sakmann, B. Local routes revisited: the space and time dependence of the Ca^{2+} signal for phasic transmitter release at the rat calyx of Held. *J. Physiol. (Lond.)* **547**, 665–689 (2003).
28. Simon, S.M. & Llinas, R.R. Compartmentalization of the submembrane calcium activity during calcium influx and its significance in transmitter release. *Biophys. J.* **48**, 485–498 (1985).
29. Augustine, G.J., Santamaria, F. & Tanaka, K. Local calcium signaling in neurons. *Neuron* **40**, 331–346 (2003).
30. Naraghi, M. T-jump study of calcium binding kinetics of calcium chelators. *Cell Calcium* **22**, 255–268 (1997).
31. Sabatini, B.L. & Regehr, W.G. Optical measurement of presynaptic calcium currents. *Biophys. J.* **74**, 1549–1563 (1998).
32. Pyle, J.L., Kavalali, E.T., Choi, S. & Tsien, R.W. Visualization of synaptic activity in hippocampal slices with FM1-43 enabled by fluorescence quenching. *Neuron* **24**, 803–808 (1999).
33. Stanton, P.K. *et al.* Long-term depression of presynaptic release from the readily releasable vesicle pool induced by NMDA receptor-dependent retrograde nitric oxide. *J. Neurosci.* **23**, 5936–5944 (2003).
34. Spacek, J. & Harris, K.M. Trans-endocytosis via spinules in adult rat hippocampus. *J. Neurosci.* **24**, 4233–4241 (2004).
35. Sturrock, R.R. Myelination of the mouse corpus callosum. *Neuropathol. Appl. Neurobiol.* **6**, 415–420 (1980).
36. Bjartmar, C., Hildebrand, C. & Loinder, K. Morphological heterogeneity of rat oligodendrocytes: electron microscopic studies on serial sections. *Glia* **11**, 235–244 (1994).
37. Trapp, B.D., Nishiyama, A., Cheng, D. & Macklin, W. Differentiation and death of premyelinating oligodendrocytes in developing rodent brain. *J. Cell Biol.* **137**, 459–468 (1997).
38. Riederer, B.M., Berbel, P. & Innocenti, G.M. Neurons in the corpus callosum of the cat during postnatal development. *Eur. J. Neurosci.* **19**, 2039–2046 (2004).
39. Temple, S. & Raff, M.C. Clonal analysis of oligodendrocyte development in culture: evidence for a developmental clock that counts cell divisions. *Cell* **44**, 773–779 (1986).
40. Carleton, A., Petreanu, L.T., Lansford, R., Alvarez-Buylla, A. & Lledo, P.M. Becoming a new neuron in the adult olfactory bulb. *Nat. Neurosci.* **6**, 507–518 (2003).
41. Ge, S. *et al.* GABA regulates synaptic integration of newly generated neurons in the adult brain. *Nature* **439**, 589–593 (2006).
42. Zhen, M. & Jin, Y. Presynaptic terminal differentiation: transport and assembly. *Curr. Opin. Neurobiol.* **14**, 280–287 (2004).
43. Li, S., Mealing, G.A., Morley, P. & Stys, P.K. Novel injury mechanism in anoxia and trauma of spinal cord white matter: glutamate release via reverse Na^{+}-dependent glutamate transport. *J. Neurosci.* **19**, RC16 (1999).
44. Kriegler, S. & Chiu, S.Y. Calcium signaling of glial cells along mammalian axons. *J. Neurosci.* **13**, 4229–4245 (1993).
45. Fields, R.D. & Burnstock, G. Purinergic signalling in neuron-glia interactions. *Nat. Rev. Neurosci.* **7**, 423–436 (2006).
46. Barres, B.A. & Raff, M.C. Proliferation of oligodendrocyte precursor cells depends on electrical activity in axons. *Nature* **361**, 258–260 (1993).
47. Demerens, C. *et al.* Induction of myelination in the central nervous system by electrical activity. *Proc. Natl. Acad. Sci. USA* **93**, 9887–9892 (1996).
48. Karadottir, R., Cavelier, P., Bergersen, L.H. & Attwell, D. NMDA receptors are expressed in oligodendrocytes and activated in ischaemia. *Nature* **438**, 1162–1166 (2005).
49. Chittajallu, R., Aguirre, A. & Gallo, V. NG2-positive cells in the mouse white and grey matter display distinct physiological properties. *J. Physiol. (Lond.)* **561**, 109–122 (2004).
50. Stricker, C. & Redman, S.J. Quantal analysis based on density estimation. *J. Neurosci. Methods* **130**, 159–171 (2003).

nature neuroscience

Vesicular release of glutamate from unmyelinated axons in white matter

Jennifer L Ziskin[1], Akiko Nishiyama[2], Maria Rubio[2], Masahiro Fukaya[3] & Dwight E Bergles[1]

Directed fusion of transmitter-laden vesicles enables rapid intercellular signaling in the central nervous system and occurs at synapses within gray matter. Here we show that action potentials also induce the release of glutamate from axons in the corpus callosum, a white matter region responsible for interhemispheric communication. Callosal axons release glutamate by vesicular fusion, which induces quantal AMPA receptor–mediated currents in NG2$^+$ glial progenitors at anatomically distinct axo–glial synaptic junctions. Glutamate release from axons was facilitated by repetitive stimulation and could be inhibited through activation of metabotropic autoreceptors. Although NG2$^+$ cells form associations with nodes of Ranvier in white matter, measurements of conduction velocity indicated that unmyelinated fibers are responsible for glutamatergic signaling with NG2$^+$ glia. This activity-dependent secretion of glutamate was prevalent in the developing and mature mouse corpus callosum, indicating that axons within white matter both conduct action potentials and engage in rapid neuron-glia communication.

The white matter of the CNS contains axons that permit functional interactions among specialized brain regions. The prevailing view is that these axons blindly transmit electrical activity through the white matter to be translated into the release of chemical messengers at synapses in gray matter; this restricted secretion of neurotransmitters at or near terminal active zones helps to maintain the specificity of intercellular communication in the nervous system[1]. Indeed, terminal boutons are rare in white matter, which contains primarily myelinated and unmyelinated axons and a variety of glial cells[2]. Nevertheless, glutamate is released in an activity-dependent manner from white matter[3], glial cells within these fiber tracts express glutamate receptors[4,5] and glutamate transporters are present to remove glutamate[6]. Furthermore, glutamate-induced excitotoxic damage to oligodendrocytes and their progenitors is often observed after ischemia[7], which leads to a loss of myelin and is a contributing factor in cerebral palsy. Despite this evidence of glutamatergic signaling in white matter, the mechanisms responsible for glutamate release within these projection pathways have not been determined.

To define the mechanisms of glutamate release within white matter, we recorded from glial precursor cells that express the proteoglycan NG2 (NG2$^+$ cells) in the corpus callosum; these cells represent a potential target of axon-derived glutamate, as they express ionotropic glutamate receptors[4], make contact with axons in white matter[8] and form synapses with neurons in the hippocampus and cerebellum[9,10]. We found that NG2$^+$ cells within the corpus callosum express functional AMPA receptors, which are activated after action potential–induced release of glutamate from unmyelinated axons. This rapid signaling occurs through vesicular fusion at defined axon–NG2$^+$ cell junctions, indicating that axons do not merely transmit electrical activity through white matter, but rather engage in rapid signaling with a distinct group of glial progenitors.

RESULTS

DsRed is expressed by NG2$^+$ cells in NG2-DsRed BAC mice

Visualization of cells within white matter using differential interference contrast (DIC) imaging is made difficult by light scattering from myelin. Therefore, to study intercellular signaling mechanisms active within NG2$^+$ cells in living tissue, we used bacterial artificial chromosome (BAC)-mediated transgenesis[11] to create mice that express the fluorescent protein DsRed under the control of the NG2 promoter. In these NG2-DsRed BAC mice, DsRed expression was restricted to NG2$^+$ cells throughout the brain, including small stellate-shaped glial cells in gray and white matter that expressed the platelet-derived growth factor receptor-α (PDGFαR) and pericytes surrounding blood vessels (**Fig. 1a–h**). To determine the proportion of NG2$^+$ cells that express DsRed in juvenile mice, we performed dual immunolabeling for NG2 and platelet-derived growth factor receptor-β (PDGFβR; to label NG2$^+$ vascular-associated pericytes) in the corpus callosum at three postnatal ages (postnatal day (P) 7, P14 and P26), and counted the number of DsRed$^+$PDGFβR$^-$ cells that were NG2$^+$ in two or three randomly selected sections in the anterior corpus callosum at the level of the striatum, and in the posterior corpus callosum at the level of the hippocampus. More than 90% of DsRed$^+$ cells were NG2$^+$ at these ages (P7: 67/70 cells, 96%; P14: 64/68 cells, 94%; P26: 57/60 cells, 95%), indicating that these BAC transgenic mice allow access to this specific population of glial progenitors in both developing and mature white matter. The small number of DsRed$^+$ cells that were NG2$^-$ had much lower DsRed fluorescence,

[1]Department of Neuroscience, Johns Hopkins University School of Medicine, 725 N. Wolfe St., WBSB 813, Baltimore, Maryland 21205, USA. [2]Department of Neurobiology and Physiology, University of Connecticut, 75 North Eagleville Road, Unit 3156, Storrs, Connecticut 06269-3156, USA. [3]Department of Anatomy, Hokkaido University Graduate School of Medicine, Sapporo, 060-8638 Japan. Correspondence should be addressed to D.E.B. (dbergles@jhmi.edu).

Received 22 December 2006; accepted 22 January 2007; published online 11 February 2007; doi:10.1038/nn1854

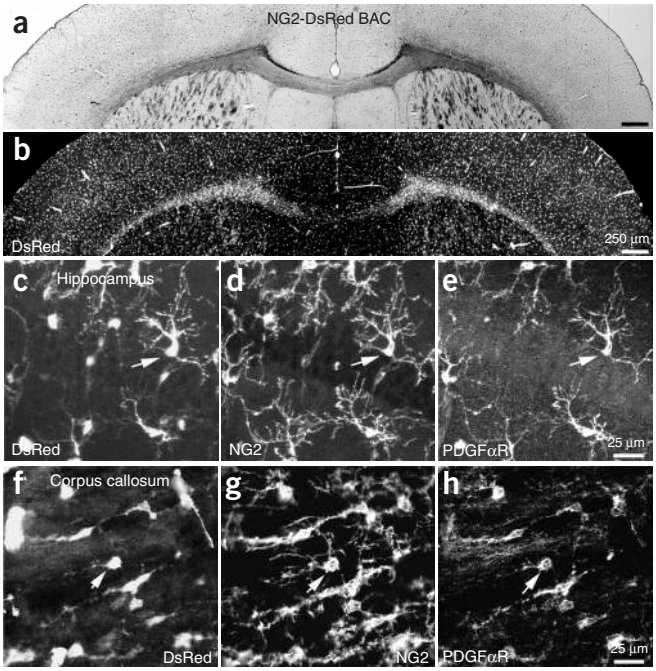

Figure 1 NG2$^+$ cells express DsRed in NG2-DsRed BAC mice. (**a**) Coronal brain section from a P24 NG2-DsRed BAC transgenic mouse. (**b**) DsRed fluorescence image from the same section as in **a**. (**c**–**e**) CA1 region of the hippocampus from a P30 NG2-DsRed BAC transgenic mouse showing DsRed fluorescence (**c**), NG2 immunoreactivity (**d**) and PDGFαR immunoreactivity (**e**). (**f**–**h**) Section of corpus callosum from the same P30 mouse showing DsRed fluorescence (**f**), NG2 immunoreactivity (**g**) and PDGFαR immunoreactivity (**h**). Arrows in each panel highlight one NG2$^+$ glial cell.

suggesting that these cells may have been transitioning to a more mature phenotype.

Glutamatergic signaling in NG2$^+$ cells within white matter

Whole-cell recordings from DsRed$^+$ glial cells in the corpus callosum revealed that these cells had a high resting potential (–101 ± 1 mV, mean ± s.e.m.), a small size (whole cell capacitance = 13.9 ± 1.5 pF) and a moderate input resistance (229 ± 59 MΩ) and did not fire action potentials in response to depolarization ($n = 13$) (**Fig. 2a**), properties similar to those of NG2$^+$ cells in gray matter[12]. Focal application of kainate to these cells triggered inward currents ($n = 11$) that were blocked by the AMPA receptor (AMPAR) antagonist GYKI 53655 (100 μM; $n = 4$), and in the majority of DsRed$^+$ cells (18/22 cells) application of NMDA elicited small currents that were blocked by the NMDA receptor (NMDAR) antagonist D,L-CPP (10 μM; $n = 5$) (**Fig. 2b** and **Supplementary Fig. 1** online). These results indicate that NG2$^+$ cells in the corpus callosum have the potential to respond to the release of glutamate.

Spontaneous inward currents were observed in callosal NG2$^+$ cells during continuous recordings that had a time course reminiscent of excitatory postsynaptic currents (EPSCs) (**Fig. 2c**) and were blocked by GYKI 53655 (10 μM; $n = 5$), indicating that their AMPARs are activated in white matter. These currents were capable of inducing small membrane depolarizations (average amplitude, 0.45 ± 0.04 mV; range, 0.17–1.55 mV; $n = 127$ events, six cells) (**Fig. 2d**). Electrical stimulation of callosal axons also triggered inward currents in NG2$^+$ cells at room temperature (22–24 °C) and near physiological temperature (36 °C), which were blocked by GYKI 53655 (100 μM; $n = 7$) (**Fig. 3a**) or the Na^+ channel antagonist tetrodotoxin (TTX, 1 μM; $n = 4$), indicating that action potentials can trigger the release of glutamate in the corpus callosum. To determine the proportion of NG2$^+$ cells that receive glutamatergic input, we randomly selected cells at three ages (P14–P15, P19–P21 and P35) and examined whether they responded to electrical stimulation of callosal fibers. EPSCs were observed in 100% (23/23 cells) of DsRed$^+$ cells at P14–P15, in 97% (32/33 cells) of DsRed$^+$ cells at P19–P21 and in 100% (12/12 cells) of DsRed$^+$ cells at P35. These results indicate that AMPAR signaling is pervasive among the population of NG2$^+$ cells in both the developing and mature corpus callosum.

When paired stimuli were applied to callosal axons with a 50-ms interstimulus interval (ISI), AMPAR responses in NG2$^+$ cells were on average much larger after the second stimulus (**Fig. 3a**); the degree of facilitation increased with age, from 1.5 ± 0.1 at P14 ($n = 5$) to 2.3 ± 0.2 at P21 ($n = 5$), after which it remained stable (at P35 the facilitation was 2.4 ± 0.1; $n = 5$). Varying the ISI from 50 to 500 ms revealed that AMPAR responses returned to control levels with a time constant of 151 ms (at P21; $n = 5$), indicating that repetitive firing of cortical neurons transiently enhances glutamate release within the corpus callosum. Furthermore, AMPAR currents became progressively larger when the stimulus intensity was increased ($n = 8$) (**Fig. 3b**), suggesting that individual NG2$^+$ cells receive glutamatergic input from multiple sources. These evoked AMPAR currents were reversibly blocked by the voltage-gated Ca^{2+} channel blocker cadmium ($CdCl_2$, 30 μM; $n = 10$) (**Fig. 3c**), indicating that Ca^{2+} influx was required to induce glutamate release. Spontaneous action potentials also were sufficient to induce glutamate release; in the presence of the $GABA_A$ receptor antagonist gabazine, bursts of AMPAR currents consisting of 2–14 events (mean, 5.6 events) appeared at regular intervals (2.0 ± 0.5 min^{-1}; $n = 4$) in callosal NG2$^+$ cells (**Fig. 3d**). Previous studies have shown that pyramidal neurons in layer II/III of the cortex, a main source of axons to the corpus callosum[13], fire bursts of action potentials at

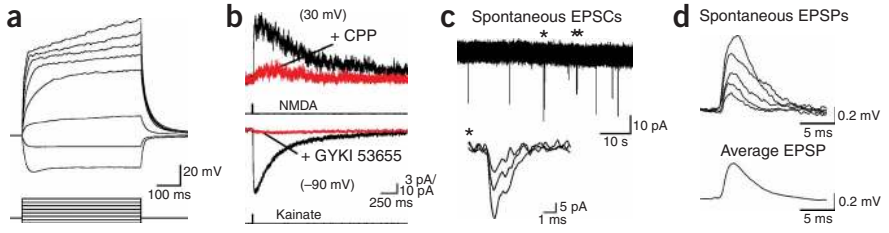

Figure 2 Spontaneous release of glutamate within the corpus callosum activates AMPA receptors in NG2$^+$ glial cells. (**a**) Whole-cell current-clamp recording from a DsRed$^+$ cell in the corpus callosum showing responses to current injection. $V_M = –97$ mV. Current steps: –90, –30, 30, 90, 150, 210, 270 and 330 pA. (**b**) Activation of NMDA receptors (upper traces) and AMPA receptors (lower traces) in DsRed$^+$ cells by focal application of NMDA (100 μM) and kainate (200 μM), respectively. NMDAR responses were blocked by D,L-CPP (upper red trace) (10 μM) and AMPAR responses were blocked by GYKI 53655 (100 μM) (lower red trace). (**c**) Spontaneous EPSCs recorded from a corpus callosum NG2$^+$ cell. Inward currents highlighted by an asterisk are shown at an expanded time scale (inset). (**d**) Individual spontaneous EPSPs recorded from an NG2$^+$ cell in current clamp (upper traces) and the average EPSP waveform calculated from 24 events (lower trace). $V_M = –104$ mV.

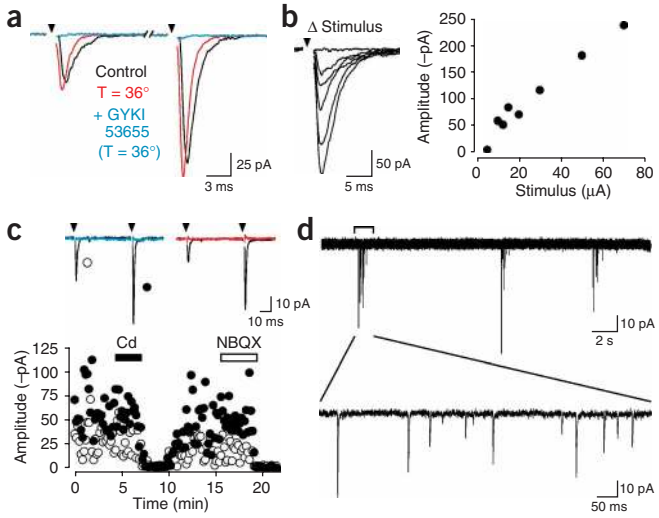

Figure 3 Stimulation of axons within the corpus callosum evokes the release of glutamate. (**a**) Response of an NG2$^+$ cell to paired stimulation of corpus callosum axons (50 ms ISI), recorded at room temperature (22–24 °C) and near physiological temperature (36 °C). Evoked responses were blocked by GYKI 53655 (100 μM). (**b**) Series of responses evoked with stimuli of different intensities (left, traces) and plot of the peak amplitude of the responses versus stimulus intensity (right, graph). Stimulation intensities: 5, 10, 12.5, 15, 20, 30, 50 and 70 μA. (**c**) Averaged responses and plot of peak amplitudes of evoked AMPAR currents recorded from an NG2$^+$ cell in response to paired stimulation. Responses were blocked by cadmium (Cd, 30 μM, blue trace) and NBQX (10 μM, red trace). Open circles, first response amplitude; closed circles, second response amplitude. (**d**) Bursts of EPSCs recorded from a callosal NG2$^+$ cell in the presence of gabazine (5 μM).

a frequency of 2–8 min^{-1} in the presence of $GABA_A$ receptor antagonists[14]. Consistent with these observations, the rhythmic bursts of AMPAR currents in NG2$^+$ cells were blocked by TTX (1 μM) ($n = 3$), indicating that intrinsically generated action potentials also induced the release of glutamate in white matter.

Glutamate release is mediated by vesicle fusion along axons

In the presence of TTX, spontaneous AMPAR currents occurred in NG2$^+$ cells at a low frequency (average, 0.008 ± 0.0085 Hz; range, 0–0.022 Hz; $n = 12$) (**Fig. 4a**). In cells that showed sufficient activity, the average amplitude of these miniature EPSCs (mEPSCs) was –18.4 ± 1.2 pA ($n = 7$). These currents had rapid rise and decay kinetics (10–90% rise time, 321 ± 25 μs; decay tau, 1.44 ± 0.13 ms; $n = 7$ cells) (**Fig. 4b**), indicating that glutamate was transiently elevated near NG2$^+$ cell AMPARs.

The neurotoxin α-latrotoxin (α-LTX) enhances Ca^{2+}-independent fusion of vesicles at glutamatergic synapses[15] by binding to specific receptors localized within axon terminal membranes[16]. Exposure to α-LTX (5 nM) similarly increased the frequency of mEPSCs in NG2$^+$ cells ($n = 3$) (**Fig. 4c**), suggesting that these events may be generated at defined synaptic junctions. Events were observed within 5–8 min of exposure to α-LTX and multiple bursts of EPSCs were typically observed in one cell. The amplitude distributions of events collected from multiple bursts were approximately unimodal, and showed a prominent skew toward larger events (**Fig. 4d**). The average peak amplitude of mEPSCs evoked with α-LTX was –15.1 ± 0.6 pA (range 14.0–16.0 pA; $n = 3$), and the coefficient of variance was 0.30 ± 0.06, comparable to the variance observed at *en passant* glutamatergic synapses in the hippocampus[17]. Previous studies have shown that the skew in the amplitude distribution of miniature events can be accounted for by the variation in vesicle size[18], assuming that the quantity of glutamate in each vesicle varies with the third power of vesicle radius, although variations in receptor occupancy and subsequent changes in unitary conductance may also influence the shape of the distribution. Indeed, when mEPSC amplitude distributions were subjected to a cubed root transformation, they were well fit with a single Gaussian ($n = 3$) (data not shown). Together, these results suggest that spontaneous AMPAR currents in NG2$^+$ cells arise from vesicular fusion along axons.

If AMPAR currents in NG2$^+$ cells are generated via fusion of glutamate-containing vesicles rather than via glutamate release through connexin hemichannels, P2X7 purinergic receptors or volume-sensitive anion channels—all channels that permit glutamate release[19]—the currents should become smaller when loading of glutamate into vesicles is inhibited. As expected for vesicular release, application of bafilomycin A1 (Baf, 2 μM), an inhibitor of the vacuolar-type ATPase

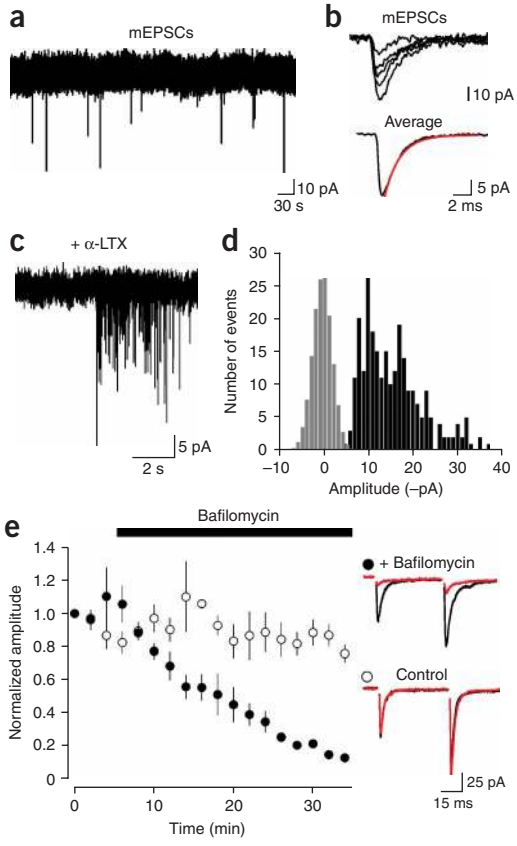

Figure 4 AMPAR currents in callosal NG2$^+$ cells arise from vesicular release of glutamate. (**a**) Spontaneous mEPSCs recorded from an NG2$^+$ cell in the presence of TTX (1 μM). (**b**) Five individual mEPSCs and the average mEPSC are shown from the recording in (**a**). The red line is a single exponential fit to the decay (tau decay = 1.6 ms). (**c**) A burst of mEPSCs recorded in an NG2$^+$ cell after exposure to α-latrotoxin (5 nM). (**d**) Graph of the amplitude distribution of α-latrotoxin induced mEPSCs (black bars) and baseline noise (gray bars, scaled to peak of mEPSC distribution). (**e**) Inhibition of glutamate loading into vesicles with the proton pump inhibitor bafilomycin A1 (Baf, 2 μM) caused a progressive decrease in evoked AMPA currents in NG2$^+$ cells. Traces at right show the average response before application of Baf (black traces) and after 30 min in the presence (red, top trace) or absence (red, bottom trace) of Baf.

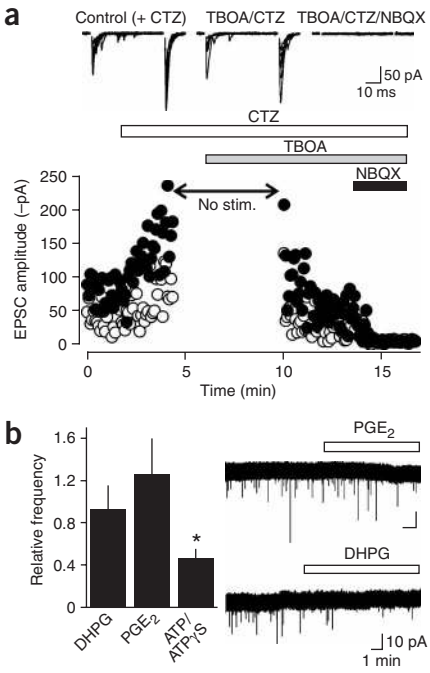

Figure 5 AMPAR currents in NG2$^+$ cells are not produced by reversed cycling of glutamate transporters or by vesicular release from astrocytes. (**a**) Evoked AMPA receptor responses persist in the presence of the glutamate transporter inhibitor TBOA (100 μM). Cyclothiazide (CTZ, 100 μM) was applied to prevent desensitization of AMPAR during uptake blockade. The stimulation was stopped during the initial application of TBOA to prevent glutamate accumulation. Traces above show ten superimposed responses to paired stimulation in the different pharmacological conditions. Open circles are the responses to the first stimulus; closed circles are the responses to the second stimulus. (**b**) Stimulation of astrocytes does not increase the frequency of mEPSCs in callosal NG2$^+$ cells. Graph shows the relative frequency (drug/control) of mEPSCs recorded after 5 min in DHPG (15 μM, $n = 11$), PGE2 (10 μM, $n = 11$) and ATP/ATPγS (100 μM, $n = 17$). Traces at the right are continuous recordings of mEPSCs showing the response of cells to PGE2 (upper trace) and DHPG (lower trace).

that establishes the voltage and pH gradients required for transport of glutamate into secretory vesicles, led to a progressive decrease in the amplitude of evoked AMPAR currents; after 30 min, the evoked response was reduced by 82 ± 3% ($n = 4$), similar to the inhibition observed at neuronal synapses[20], while responses recorded without Baf decreased by only 25 ± 6% ($n = 4$) (**Fig. 4e**). The Baf-induced reduction could not be accounted for by changes in the responsiveness of NG2$^+$ cells to glutamate, as kainate-evoked currents were reduced by only 27 ± 7% ($n = 4$) by Baf over this period. The rapid kinetics of the AMPAR currents, and the dependence of release on voltage-gated Ca^{2+} channels and vesicle filling, suggest that action potentials rapidly trigger the fusion of glutamate-filled vesicles along axons within the corpus callosum.

It has been reported that axons in optic nerve can release glutamate through reversed cycling of glutamate transporters[3]. This mechanism of release is inconsistent with the rapid kinetics of the AMPAR currents observed in callosal NG2$^+$ cells, because transporters cycle slowly[21] and are expressed at a low level in axonal membranes. Indeed, evoked AMPAR currents in NG2$^+$ cells could still be elicited in the presence of the glutamate transporter antagonist D,L-*threo*-β-benzyloxyaspartate (TBOA, 100 μM; $n = 5$) (**Fig. 5a**), when cyclothiazide (CTZ, 100 μM) was included to prevent AMPAR desensitization by elevated ambient glutamate. The decay kinetics of evoked EPSCs were not altered by TBOA (tau decay; control (CTZ), 1.99 ± 0.19 ms; TBOA (CTZ), 2.18 ± 0.19 ms; $n = 12$, $P = 0.068$), in accordance with the limited role of transporters in shaping AMPAR EPSCs at synapses containing a single release site[22]. However, TBOA decreased the amplitudes of EPSCs by 69 ± 4% ($n = 12$) (control (CTZ), –128 ± 20 pA; TBOA (CTZ), –39 ± 9 pA). This depression could have resulted from tonic activation of AMPARs or activation of 'presynaptic' metabotropic glutamate receptors (mGluRs) at sites of release. Application of the mGluR agonist (±)-1-aminocyclopentane-*trans*-1,3-dicarboxylic acid (*trans*-ACPD) caused a 76 ± 4% ($n = 4$) reduction in the amplitude of evoked responses; in three cells that showed failures before *trans*-ACPD application, this reduction was accompanied by a 4.2 ± 1.5–fold increase in failures, indicating a presynaptic site of action. These results suggest that mGluR autoreceptors are present along axons in white matter to regulate glutamate release.

Astrocytes in gray matter areas such as the hippocampus can release glutamate through Ca^{2+}-dependent vesicular fusion in response to neuronal activity[23]. Although tetanic stimulation is required to initiate glutamate secretion from astrocytes, and this release occurs tens of seconds after the stimulus, it is nevertheless possible that astrocytes rather than axons could be the source of glutamate in white matter. However, although stimulation of receptors that elicit glutamate release from astrocytes, including metabotropic receptors (DHPG, 15 μM; $n = 11$), purinergic receptors (ATP, 100 μM; $n = 17$) and prostaglandin receptors (PGE2, 10 μM; $n = 11$), was sufficient to induce a Ca^{2+} rise in astrocytes within the corpus callosum (data not shown) (see **Supplementary Methods** online), it did not increase the frequency of spontaneous miniature AMPAR currents in white matter NG2$^+$ cells (**Fig. 5b**). The frequency of mEPSCs in NG2$^+$ cells was significantly reduced by ATP ($P = 0.004$) but not by DHPG ($P = 0.078$) or PGE2 ($P = 0.809$). ATP also decreased the amplitude of evoked responses by 63 ± 9% ($n = 6$), which was accompanied by a more than threefold increase in failures ($P < 0.01$), indicating that ATP also reduces the probability of glutamate release from axons in white matter.

Glutamate release in developing and mature white matter

The quantal currents seen in NG2$^+$ cells could be generated at transient contacts between growing axons and glia, as neurotransmitters can be released from growth cones[24] and non-neuronal guidepost cells serve as interim targets for growing axons[25]. Although NG2$^+$ cells appear in the corpus callosum before birth, evoked AMPAR currents were not observed in these cells until P5. These responses were small in young mice (P7–P9; amplitude range, –5 to –30 pA; $n = 4$), but increased in size as the animals matured (P20–30; amplitude range, –40 to –400 pA; $n = 15$) and could be elicited in NG2$^+$ cells in the corpus callosum of adult (P90) mice ($n = 5$) (data not shown). Thus, rapid signaling between axons and glia is established early and persists into adulthood, paralleling the maturation of this white matter tract. Could this signaling occur as a result of interactions at the ends of severed axons? To address this possibility we recorded from NG2$^+$ cells near the midline of coronal slices where the corpus callosum had been completely severed; if axotomy induces the *de novo* formation of junctions between NG2$^+$ cells and axons, the frequency of miniature events should be higher within these regions than in cells located within untransected slices. The frequency of miniature events was not significantly different in cells located near the transected area (control: 0.008 ± 0.0085 Hz, $n = 12$; transected: 0.010 ± 0.011 Hz, $n = 11$, $P > 0.05$), indicating that AMPAR currents do not reflect vesicle fusion at the ends of severed axons.

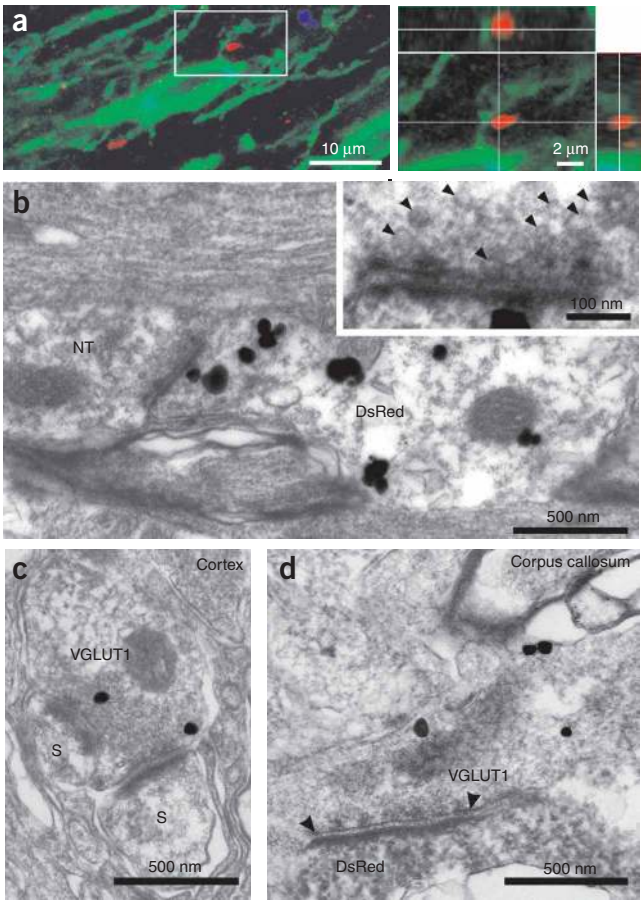

Figure 6 Axons form defined synaptic junctions with NG2$^+$ cells within the corpus callosum. (**a**) Triple-immunofluorescence of NG2 (green), VGLUT1 (red) and Map2 (blue) immunoreactivity in a projection image showing close association between VGLUT1$^+$ puncta and NG2$^+$ processes; these VGLUT1$^+$ puncta were not in close proximity to neuronal dendrites (blue process, left image). The area circumscribed by the white box is shown in an orthogonal reconstruction with *x-z* and *y-z* planes extracted at the levels indicated by the white lines (right). (**b**) Thin-section electron micrograph from the corpus callosum. Silver-enhanced pre-embedding immunogold for DsRed shows an NG2$^+$ cell process (DsRed) opposed to a nerve terminal (NT) containing small clear vesicles. The inset shows the active zone region at higher magnification, illustrating the region of close apposition between axon and NG2$^+$ cell membranes, the accumulation of electron-dense material, and the presence of small (~35-nm-diameter) vesicles in the axon. (**c**) Thin-section electron micrograph from the cortex showing VGLUT1 immunoreactivity (silver-enhanced immunogold, VGLUT1) in a terminal bouton that forms two synapses with dendritic spines (S). (**d**) Thin-section electron micrograph from the corpus callosum showing VGLUT1 immunoreactivity (silver-enhanced immunogold, VGLUT1) in an axon that forms a synaptic junction (highlighted by arrowheads) with a lightly labeled NG2$^+$ cell process (DsRed immunoreactivity, horseradish peroxidase product).

If each axon makes only one junction with an NG2$^+$ cell, and only one vesicle is released at a time at these sites, then the quantal content of evoked EPSCs provides a lower bound for the number of axons that provide input to NG2$^+$ cells. Dividing the average maximum amplitude of EPSCs elicited through paired stimulation (–203 ± 44 pA, $n = 8$) by the average mEPSC amplitude (–18.4 ± 1.2 pA) indicates that, on average, NG2$^+$ cells in the mature corpus callosum receive input from 11 fibers. This is a conservative estimate, as not all inputs may have released glutamate in response to the stimulus.

Synaptic junctions between NG2$^+$ cells and callosal axons

To determine whether anatomically distinct synaptic junctions are formed with NG2$^+$ cells in the corpus callosum, we performed immunolabeling for NG2 and the type 1 vesicular glutamate transporter (VGLUT1). Discrete VGLUT1$^+$ puncta were observed throughout the corpus callosum that were also immunoreactive for synaptophysin (**Supplementary Fig. 2** online), indicating that there are numerous sites of vesicle accumulation within glutamatergic axons that project through this region. In many instances, VGLUT1$^+$ puncta were directly apposed to NG2$^+$ processes; of 15 NG2$^+$ cells examined, 14 had processes with associated VGLUT1$^+$ puncta (mean, 5.7 ± 1.5 puncta per cell; range, 0–23 puncta; $n = 15$) (**Fig. 6a**). Notably, these sites of VGLUT1 accumulation were not adjacent to microtubule-associated protein-2–expressing dendrites, indicating that NG2$^+$ cells are a direct target of callosal axons (**Supplementary Fig. 2**).

To determine the ultrastructural relationships between nerve fibers and NG2$^+$ cell processes, we visualized DsRed in NG2-DsRed BAC mice using silver-enhanced pre-embedding immunogold. In accordance with the accumulation of VGLUT1 next to NG2$^+$ cell processes, discrete junctions were observed between axons and DsRed$^+$ cell membranes that showed the structural characteristics of neuronal synapses, including rigid parallel apposition of axonal and NG2$^+$ cell membranes, accumulation of small, clear vesicles near the pre-junctional membrane, electron-dense material in the extracellular space separating the two membranes, and localization of mitochondria in the pre-junctional axon ($n = 19$ junctions, five cells) (**Fig. 6b**). The length of active zones at these sites was more variable than that observed for synapses in layer VI of the cortex (corpus callosum: 280 ± 142 nm, $n = 17$; cortex: 264 ± 43 nm, $n = 17$; $P = 0.895$), although the average length was similar. Immunogold labeling revealed that these axons contained VGLUT1, and vesicles observed within axons at these junctions had the same diameter as those at cortical synapses (corpus callosum: 35 ± 5 nm, $n = 30$ vesicles; cortex: 36 ± 4 nm, $n = 49$ vesicles; $P = 0.207$) (**Fig. 6c**,**d**). These results indicate that axons in white matter form specialized junctions with NG2$^+$ cells that share many structural similarities with conventional synapses in the gray matter.

Vesicular release from unmyelinated axons in white matter

NG2$^+$ cells within the optic nerve and spinal cord make contact with nodes of Ranvier[8,26], raising the possibility that vesicle secretion is localized to nodal regions of myelinated axons. However, approximately 30% of axons in the adult rodent corpus callosum are unmyelinated[27]. To determine which axons were responsible for glutamate release in white matter, we estimated the conduction velocity of axons that mediate NG2$^+$ cell AMPAR currents. Increasing the separation between the stimulating electrode and the cell resulted in a substantial increase in the delay between the stimulus and the onset of the response (**Fig. 7a**). A regression of the delay measured at various distances provides an estimate of the conduction velocity of the axons responsible for generating the AMPAR currents. For seven NG2$^+$ cells, the mean conduction velocity was 0.45 ms^{-1} (at 37 °C) (**Fig. 7b**). Similar time-delay measurements of EPSCs elicited in hippocampal CA1 pyramidal neurons indicated that Schaffer collateral fibers had a conduction velocity of 0.18 ms^{-1}, in agreement with the small diameter of these unmyelinated axons[28]. To compare these measurements to the conduction velocity of myelinated and unmyelinated axons in the corpus callosum of NG2-DsRed BAC mice, we recorded evoked extracellular compound action potentials (CAPs) produced by these

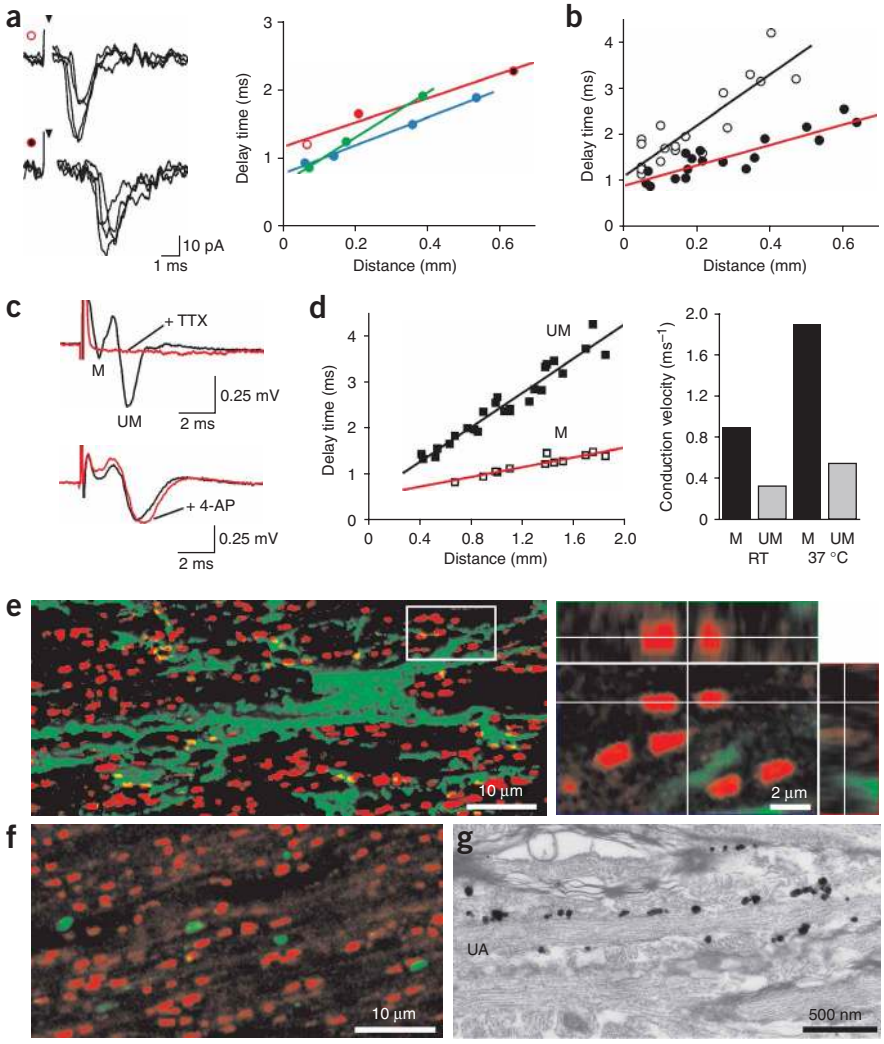

Figure 7 Glutamate is released from unmyelinated axons in the corpus callosum. (**a**) Left, example traces recorded from an NG2$^+$ cell after callosal axon stimulation at distances of 70 µm (upper traces, open red circle) and 640 µm (lower traces, filled red circle). Inverted arrowhead denotes time of stimulation. Right, plot of change in delay between stimulation and onset of EPSC recorded with increasing separation of stimulation electrode and NG2$^+$ cell. Each color corresponds to responses of one cell; red circles correspond to the traces shown at left. (**b**) Plot of delay time versus distance for synaptic responses recorded from 7 callosal NG2$^+$ cells (filled circles, red line) and 13 hippocampal CA1 pyramidal neurons (open circles, black line). Lines represent regression fits to the points (P33–P51 NG2$^+$ cells; P20–P33 pyramidal neurons). (**c**) Extracellular recordings of compound action potentials (CAPs) generated by myelinated (M) and unmyelinated (UM) fibers in the corpus callosum, showing the sensitivity to TTX (1 µM) and 4-aminopyridine (4-AP, 10 µM) (lower red trace). (**d**) Left, plot of delay time versus distance for myelinated (M, open squares) and unmyelinated (UM, filled squares) fibers at 37 °C. Right, conduction velocities of myelinated and unmyelinated fibers calculated from extracellular CAPs. Ages for **c** and **d** were P32–P37. (**e**) Double-immunofluorescence for NG2 (green) and Caspr (red) shown in a projection image with isosurface rendering of the NG2$^+$ cell (left). The area circumscribed by the white box is shown in an orthogonal reconstruction with *x-z* and *y-z* planes extracted at levels indicated by the white lines (right). Age, P30. (**f**) Double-immunofluorescence for Caspr (red) and VGLUT1 (green) shown in a projection image. (**g**) Silver-enhanced pre-embedding immunogold for DsRed showing extensive contact between an unmyelinated axon (UA) and DsRed$^+$ processes in the corpus callosum. Age, P35.

fiber tracts; CAPs produced by the two groups of fibers can be distinguished by differences in conduction velocity and by sensitivity to 4-aminopyridine (4-AP), which preferentially slows the conduction of unmyelinated fibers[29]. Two discrete negative waves were visible in the field response after callosal stimulation, which were blocked by TTX (1 µM, $n = 6$) (**Fig. 7c**); the second CAP peak was prolonged by 4-AP (10 µM; $n = 5$), indicating that it reflected the activity of unmyelinated fibers. Time-delay measurements revealed that the conduction velocity of myelinated fibers was 0.89 ms^{-1} at room temperature, whereas that of unmyelinated fibers was 0.33 ms^{-1}. At 37 °C these values increased to 1.89 ms^{-1} (myelinated fibers) and 0.54 ms^{-1} (unmyelinated fibers) (**Fig. 7d**), comparable to conduction velocities measured in the rat corpus callosum[29]. The slow conduction velocity of axons giving rise to EPSCs in NG2$^+$ cells (0.45 ms^{-1}) suggests that glutamate is released primarily from unmyelinated fibers.

The involvement of unmyelinated axons in this axon-glia signaling indicates that NG2$^+$ cell–axon interactions are not limited to the nodes of Ranvier. Indeed, visualization of the paranodal protein Caspr revealed that the majority of nodes (67 ± 3%) in the vicinity of NG2$^+$ cells were not associated with NG2$^+$ cell processes ($n = 731$ nodes, 3 cells) (**Fig. 7e** and **Supplementary Fig. 2**); because NG2$^+$ cells cover only a small portion of the corpus callosum, these results indicate that few nodes are associated with NG2$^+$ cells. Furthermore, analysis of 515 VGLUT1$^+$ puncta in four coronal sections of corpus callosum revealed that only 2 ± 1% of the VGLUT1$^+$ puncta were located near nodes (**Fig. 7f**). In contrast to the limited interaction between nodes and NG2$^+$ cells, DsRed immunogold labeling revealed large areas of contact between NG2$^+$ cells and unmyelinated nerve fibers in this region (**Fig. 7g**). These results, and the finding that evoked AMPAR currents could be elicited in NG2$^+$ cells for >1 h with repeated stimulation (at 0.25 Hz), indicate that glutamate is released from unmyelinated axons within the corpus callosum at defined axon-glia synaptic junctions.

Previous studies have demonstrated that NG2$^+$ cells in the hippocampus and cerebellum express Ca^{2+}-permeable AMPARs[9,10]. To determine whether AMPAR signaling in white matter NG2$^+$ cells could also enable Ca^{2+} influx, we measured the rectification of evoked EPSCs with 100 µM spermine in the intracellular solution, which blocks outward current through Ca^{2+}-permeable AMPARs. In the developing corpus callosum (P7–P8), the current-to-voltage (*I-V*) relationship of NG2$^+$-cell EPSCs showed little deviation from linearity at positive potentials ($n = 4$) (**Fig. 8a**), suggesting that few Ca^{2+}-permeable AMPARs were activated. In contrast, in the mature corpus callosum (P42–P52) the *I-V* relationship showed prominent inward rectification ($n = 8$) (**Fig. 8b**), with the amplitudes of evoked EPSCs being proportionally smaller at positive potentials. This rectification was not observed when spermine was omitted from the intracellular

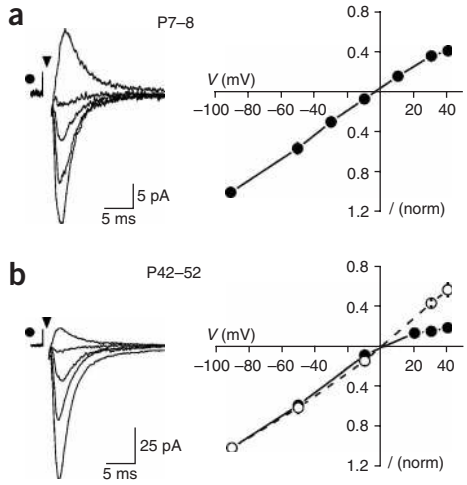

Figure 8 NG2$^+$ cells in the adult corpus callosum express Ca^{2+}-permeable AMPARs. (**a**) Evoked EPSCs recorded from an NG2$^+$ cell in the developing corpus callosum (P8) with an internal solution containing spermine (left traces) at holding potentials of –90, –50, –10 and 30 mV. At right is the current-voltage (*I-V*) relationship of AMPAR currents elicited in NG2$^+$ cells in young animals (P7–P8) ($n = 4$). These responses showed little rectification, indicating that few Ca^{2+}-permeable AMPARs were activated. (**b**) Evoked EPSCs recorded from an NG2$^+$ cell in the mature corpus callosum (P52) with an internal solution containing spermine (left traces) at holding potentials of –90, –50, –10 and 30 mV. At right is the *I-V* relationship of AMPAR currents elicited in NG2$^+$ cells in mature animals (P42–P52), when spermine was present (filled circles, $n = 8$)) or absent (open circles, $n = 3$) from the internal solution. Responses at this age showed prominent inward rectification, indicating that Ca^{2+}-permeable AMPARs contributed to the EPSCs.

solution, indicating that vesicular release of glutamate from axons in the mature corpus callosum results in the activation of Ca^{2+}-permeable AMPARs in NG2$^+$ cells. The small depolarization produced by spontaneous EPSPs (**Fig. 2**) suggest that the flux of Ca^{2+} through these receptors may be essential for regulating the behavior of NG2$^+$ cells.

DISCUSSION

Here we investigated the mechanisms responsible for glutamate release within the corpus callosum, an expanse of white matter that is the principal commissural pathway linking the two cerebral hemispheres. We found that the propagation of action potentials through this region induces the secretion of glutamate from unmyelinated axons. This vesicular release of glutamate results in the transient activation of AMPARs in NG2$^+$ cells, a distinct class of glial progenitor cells that make overt synaptic junctions with this subset of axons. Thus, axons in white matter not only convey information to other gray matter regions but also engage in rapid synaptic signaling with glial cells. The presence of numerous sites of vesicular release in white matter has implications both for activity-dependent control of myelination and for the mechanisms responsible for ischemia-induced excitotoxic damage to myelin.

Callosal axons arise primarily from pyramidal neurons in layers II/III and V and are purely excitatory[13]. Although unmyelinated axons comprise up to 30% of the axons that traverse this commissure, remarkably little is known about the information carried by these fibers. Because of their small diameter and lack of myelin sheaths, they conduct action potentials up to 40 times more slowly than the most rapidly conducting myelinated fibers. Therefore, in humans, events initiated in one hemisphere that are conveyed by these fibers would arise in the contralateral cortex with a delay of about 200 ms, assuming that unmyelinated axons conduct action potentials at 0.5 ms^{-1} over a length of 0.1 m. Whereas large myelinated fibers in the corpus callosum arise from primary sensory regions, unmyelinated axons arise from and project to prefrontal association areas, which may have less stringent requirements for temporal and spatial summation of inputs[30]. It has been suggested that these fibers may even exert a tonic rather than a phasic influence on their targets[30]. As our results indicate that these unmyelinated fibers are a primary source for the release of glutamate within the corpus callosum, it is possible that they may have a greater role than myelinated fibers in influencing the behavior of glial cells; neuron–glial cell signaling may not require the precise timing that is critical for interactions among neurons.

Oligodendrocyte progenitors within white matter express NG2, a chondroitin sulfate proteoglycan that regulates cell proliferation and motility[31] and axon growth[32,33] and prevents axon regeneration[34]. Within these cells, NG2 is directly coupled to AMPARs through an interaction with the scaffolding protein GRIP1 (ref. 35). AMPARs in these progenitors may therefore attract NG2-bearing processes to particular regions of unmyelinated axons, in a manner analogous to that demonstrated for Bergmann glial cells in the cerebellum[36], to create a matrix that helps to maintain callosal projections and prevent sprouting. In addition, *in vitro* studies have shown that AMPAR signaling in NG2$^+$ progenitors can regulate the ability of these cells to differentiate into myelinating oligodendrocytes[37]. This widespread glutamatergic signaling between axons and oligodendrocyte progenitors in the corpus callosum could therefore allow axons to influence the extent of myelination within white matter[38], which has been shown to vary with both development and behavioral experience[39]. Although our studies indicate that glutamate is released at these axon-glia junctions, it is also possible that other neurotransmitters—such as ATP, which has also been implicated in activity-dependent regulation of myelination[40]—could be concurrently released at these sites. If activity could initiate myelination of these fibers, there would be a marked increase in the speed of information transfer between cortical associational areas.

Despite the demonstrated role of NG2$^+$ cells in the formation of oligodendrocytes, these cells are abundant outside white matter areas, a finding that has led to the proposal that NG2$^+$ cells may comprise a diverse population of cells that perform distinct functions and are destined for different fates. Indeed, comparisons of NG2$^+$ cell properties across various white and gray matter regions have uncovered variations in cell morphology[41], physiological properties[42] and patterns of gene expression[43]. Nevertheless, our studies indicate that in the mature CNS, NG2$^+$ cells in the gray and white matter share some physiological properties, including a high resting membrane potential, expression of voltage- and ligand-gated ion channels, and a lack of excitability. Furthermore, NG2$^+$ cells in both white and gray matter engage in glutamatergic signaling with neurons, indicating that this rapid form of neuron-glia communication is a universal property of this class of glial cells. The fact that this signaling is not restricted to myelinated regions[10] suggests that activity at these synapses may influence more than oligodendrogenesis, and that NG2$^+$ cells may have ongoing roles in influencing the organization or activity of neuronal projections throughout the CNS.

Cerebral ischemia often causes extensive damage to oligodendrocytes and their progenitors, leading to a loss of myelin[44]. In gray matter, ischemic episodes trigger widespread, sustained fusion of synaptic vesicles, which contributes to the increase in extracellular glutamate that is responsible for excitotoxicity[45]. In experimental ischemia, white matter injury is ameliorated by administration of AMPAR

antagonists[7], indicating that excitotoxicity is also responsible for damage to glia in these regions. $NG2^+$-cell AMPARs represent one site of action for these drugs. In addition, the presence of $VGLUT1^+$ puncta at axon–$NG2^+$ cell junctions suggests that vesicular fusion at these sites may contribute to glutamate release in white matter during ischemia.

Recent studies have provided evidence that NMDARs are also expressed by oligodendrocytes and their precursors in white matter and contribute to ischemic injury to myelin[5,46]. However, we found that NMDARs are expressed by only ~60% of $NG2^+$ cells in the developing and mature corpus callosum, and NMDAR currents from these cells were very small (~10 pA at 30 mV) under saturating conditions (see **Supplementary Fig. 1**). Assuming a unitary conductance of 50 pS and a maximum open probability of 0.3 (ref. 47), these results suggest that ~20 NMDARs were present in each cell. $NG2^+$ cells may be extraordinarily sensitive to the Ca^{2+} that flows through these receptors; however, we found that ~40% of $NG2^+$ cells had no detectable NMDAR current. Furthermore, NMDAR currents in $NG2^+$ cells were blocked by Mg^{2+} at their resting potential, indicating that substantial depolarization would be required to allow Ca^{2+} influx through these receptors. These results suggest that NMDAR antagonists may offer limited protection of oligodendrocyte progenitors during ischemia. Further knowledge about the complement of receptors expressed by white matter $NG2^+$ cells, and the regulation of synaptic transmission between axons and this class of progenitors, may offer new avenues for the prevention of myelin damage after ischemic injury or in demyelinating diseases.

METHODS

Generation of BAC transgenic mice. Transgenic mice expressing DsRed-T1 under the control of the NG2 promoter were generated using BAC-mediated transgenesis[11]. The DsRed-T1 coding sequence and rabbit β-globin polyadenylation signal were inserted into the first exon of the mouse NG2 gene, immediately 5′ to the translation initiation site, in a BAC clone by homologous recombination in *Escherichia coli*. The ATG of the translation initiation site was mutated to AAG to allow translation from the first ATG in the DsRed cDNA. Clones were analyzed by PCR and Southern blotting to confirm insertion and correct orientation of the transgene. The modified BAC DNA was linearized and microinjected into the pronucleus of fertilized oocytes from B6SJL/F1 mice at the John Hopkins University Transgenic Facility. Three founders were identified by PCR analysis using primers from the DsRed sequence, which showed the same pattern of DsRed expression, but varied in the amount of DsRed expressed.

Slice preparation. Coronal cerebral brain slices were prepared from postnatal (P5–P90) NG2-DsRed mice using standard techniques, in strict accordance with a protocol approved by the Animal Care and Use Committee at Johns Hopkins University. Slices 250 μm thick were cut with a vibratome using a sapphire blade in ice cold *N*-methyl-D-glucamine (NMDG)-based cutting solution containing 135 mM NMDG, 1 mM KCl, 1.2 mM KH_2PO_4, 20 mM choline bicarbonate, 10 mM glucose, 1.5 mM $MgCl_2$ and 0.5 mM $CaCl_2$. Slices were maintained thereafter in artificial cerebral spinal fluid (ACSF) containing 119 mM NaCl, 2.5 mM KCl, 2.5 mM $CaCl_2$, 1.3 mM $MgCl_2$, 1 mM NaH_2PO_4, 26.2 mM $NaHCO_3$ and 11 mM glucose. Slices were maintained in ACSF at 37 °C for 30 min, and thereafter at room temperature. ACSF was bubbled with 95% O_2/5% CO_2. Unless noted, all experiments were carried out at room temperature. $NG2^+$ cells were visualized on an upright microscope (Zeiss Axioskop FS2) equipped with both DIC optics and a filter set for visualizing DsRed fluorescence (HQ:TRITC 41002c, Chroma) using a ×40 water-immersion objective (Zeiss Acroplan 40x IR) and two charge-coupled device (CCD) cameras (Sony XC-73 and XC-EI30). Two CCD camera controllers (Hamamatsu C-2400) were used to adjust image quality and an image combiner (MicroImage PIX/2) was used to display DIC and fluorescence signals simultaneously.

Electrophysiology. Whole-cell recordings were made from callosal $NG2^+$ cells in ACSF using conventional techniques. The electrode solution consisted of 100 mM $CsCH_3SO_3H$ (CsMeS), 20 mM tetraethylammonium (TEA) chloride, 20 mM HEPES, 10 mM EGTA, 2 mM sodium ATP and 0.2 mM sodium GTP (pH 7.3). The membrane resistance of $NG2^+$ cells was >1 GΩ when recordings were made with this solution. For current-clamp recordings, we replaced CsMeS with KCH_3SO_3H (KMeS) in the electrode solution and omitted TEA. Pipette resistance varied from 3.5 to 4.5 MΩ and recordings were made without series resistance compensation. Membrane potentials have been corrected for the error resulting from the liquid junction potentials, and unless otherwise noted, the holding potential was −90 mV. Evoked responses were elicited using a bipolar stainless steel electrode (Frederick Haer Co.; tip separation, 150 μm) placed within the corpus callosum. Stimuli varied between 5 and 200 μA and were 80–200 μs in duration. In some experiments, the temperature of the superfusing solution was increased using a feedback-controlled in-line heater (Warner Instruments). Baf was applied by recirculating continuously oxygenated ACSF containing the drug using a peristaltic pump (Instech Laboratories). For analysis of astrocyte modulation (**Fig. 5b**), ruthenium red was included in some recordings to enhance the frequency of mEPSCs in $NG2^+$ cells. For extracellular field recordings of CAPs, 450-μm-thick slices were prepared. Extracellular field electrodes of a tip resistance of 1.5–2.5 MΩ were filled with ACSF and CAPs were evoked using constant current (50–300 μA).

The following agents were applied by addition to the superfusing ACSF: TTX (Alomone Lab or Tocris), 1 μM; CTZ (Tocris), 100 μM; GYKI 53655 (Sigma), 100 μM; 2,3-dihydroxy-6-nitro-7-sulfamoyl-benzo(*f*)quinoxaline (NBQX; Tocris), 10 μM; ruthenium red (Sigma), 100 μM; gabazine (SR-95531; Tocris), 5 μM; DHPG (Tocris), 15 μM; PGE2 (Biomol), 10 μM; bafilomycin A1 (Biomol), 2 μM; TBOA (Tocris), 100 μM; CPP (Tocris), 10 μM; ATP/ATPγS (Sigma), 100 μM; D-serine (Aldrich), 50 μM; Cd^{2+} ($CdCl_2$; Aldrich), 30 μM; kainate (Tocris), 30 μM; NMDA (Tocris), 200 μM; and D-aspartate (Sigma), 100 μM.

Analysis. Responses were recorded using a MultiClamp 700A amplifier (Axon Instruments), filtered at 2 kHz, digitized at 50 kHz and recorded to disk using pClamp9 software (Axon Instruments) or stored continuously to tape (CDAT-4, Cygnus Technology). Data were analyzed offline using Clampfit (Axon Instruments), Origin (OriginLab Corp.) and Mini analysis (Synaptosoft Inc.) software. Data are expressed as mean ± s.e.m., and statistical significance was determined using the unpaired Student's *t*-test with a cutoff value of 0.05. The paired pulse ratio (PPR) is reported as the ratio of the peak amplitude of the second response (P2) to the peak amplitude of the first response (P1). The decay time of events was measured by fitting the response with a single exponential using the logistic equation. Amplitude histograms of mEPSCs were plotted using 1-pA bins and Gaussian fits were generated in Origin software. Stimulus artifacts have been truncated for clarity.

Histology. Mice were anesthetized with pentobarbital and perfused with 4% paraformaldehyde in 0.1 M sodium phosphate buffer containing 0.2% (wt/vol) picric acid in accordance with a protocol approved by the Animal Care and Use Committee at Johns Hopkins University. Brain tissue was isolated and maintained in this solution for 6–18 h at 4 °C, then washed in phosphate buffer. Tissue was cut into 30–50-μm sections on a vibrotome, or cryoprotected in sucrose and frozen with 2-methylbutane in OCT compound (Electron Microscopy Sciences) for sectioning at 20 μm on a cryostat (Zeiss; 500OM). For labeling, free-floating sections or slide-mounted sections were treated with 0.3% Triton X-100, and nonspecific antibody reaction was blocked with 5% donkey serum. Rabbit and guinea pig antibodies to NG2 were used at 1:1,000 and rabbit antibody to PDGFαR at 1:200 (see Acknowledgments for sources)[48]. Antibodies to NG2 label both $NG2^+$ glial cells and perivascular cells. The guinea pig antibody to Caspr (see Acknowledgments)[49] was used at 1:1,500, the antibody to Map2 was used at 1:500 (Sigma) and the goat and guinea pig antibodies to VGLUT1 IgG were used at 2.0 μg ml^{-1}. The rabbit antibody to synaptophysin[50] was used at 1 μg ml^{-1}. Immunoreactivity to different antigens was detected with Alexa 488– (Molecular Probes), Cy2-, Cy3- or Cy5-conjugated secondary antibodies to rabbit, mouse, goat or guinea pig (1:500; Jackson ImmunoResearch). Fluorescence images were collected with a Noran Oz confocal microscope (Noran) attached to an upright microscope (Zeiss Axioskop FS2) using a ×40 water-immersion objective, Kr-Ar (488 nm, 568 nm) and red HeNe (633 nm) lasers, and Cy2 (500–550-nm band-pass), Cy3 (590-nm band-pass) and Cy5 (660-nm long-pass) filter sets. Low-power images were obtained using a Nikon Eclipse E800 microscope with a Q Imaging Retiga EX

camera. Control sections incubated with secondary antibody alone did not result in labeling of cells. Images shown in **Figures 6** and **7** and **Supplementary Figure 2** were collected with a LSM 510 Meta confocal microscope (Zeiss) using ×40 or ×63 oil immersion objectives and 488-nm, 543-nm and 633-nm laser lines and were filtered using 500–530-nm band-pass, 565–615-nm band-pass and 644–719-nm meta detector setting. *Z*-stack images were taken at 0.5-μm intervals. The projection images shown in **Figures 6a** and **7f** are composed of five serial sections. All orthogonal images were created from six serial sections. The projection image in the left panel of **Figure 7e** is composed of nine serial images; isosurface rendering of NG2 immunoreactivity was performed using Imaris software with an edge preserving filter width set at 0.097 μm, an intensity threshold of 37.992 and a voxel size of 0.4061 × 0.4061 × 0.8 μm. This rendering of the $NG2^+$ cell prevented the inappropriate appearance of colocalization between nodes and $NG2^+$ cell processes in the combined image.

Electron microscopy. For pre-embedding immunoelectron microscopy, adult NG2-DsRed-BAC mice were perfused transcardially with 4% paraformaldehyde/0.1% glutaraldehyde in 0.1 M PB under deep pentobarbital anesthesia. After blocking with 5% BSA in TBS/0.02% saponin (blocking solution), coronal sections (50 μm in thickness) including corpus callosum were incubated overnight with rabbit anti-DsRed IgG (1:2,000, BD Bioscience) and then with anti-rabbit IgG conjugated to 1.4-nm gold particles (Nanoprobes). Following silver enhancement (HQ silver, Nanoprobes), sections were osmificated, dehydrated and embedded in Epon 812 resin. For double immunoelectron microscopy, sections were first subjected to silver-enhanced immunogold for DsRed, and then to immunoperoxidase for VGLUT1 using guinea pig anti-VGluT1 IgG (2.0 μg ml^{-1}), SAB-PO kit (Nichirei) and 3,3′-diaminobenzidine (Sigma). Ultrathin sections were prepared with an ultramicrotome (Leica Ultracut UCT) and stained with 2% uranyl acetate. Electron micrographs were taken with an H-7100 electron microscope (Hitachi).

Note: Supplementary information is available on the Nature Neuroscience website.

ACKNOWLEDGMENTS

We thank N. Heintz (Columbia University, New York) for providing BAC cloning reagents, B. Glick (University of Chicago) for the DsRed-T1 cDNA, W.B. Stallcup (Burnham Institute, San Diego) for antibodies to NG2 and PDGFαR, M.H. Bhat (University of North Carolina, Chapel Hill) for antibodies to Caspr, R. Edwards (University of California, San Francisco) for $VGLUT1^{+/+}$ and $VGLUT1^{-/-}$ tissue, N. Nishiyama for assistance with PCR and mouse breeding, the IVAX Drug Research Institute for GYKI 53655, G. Ellis-Davies for MNI-D-aspartate, M. Watanabe for support and comments on the manuscript, J. Egen for assistance with confocal imaging and image analysis, and P. Somogyi for comments on the manuscript. This work was supported by the US National Institutes of Health grants NS051509 (D.E.B.), PAR-02-059 (D.E.B.) and NS049267 (A.N.), as well as by the March of Dimes (D.E.B.), NARSAD (D.E.B.), the National Multiple Sclerosis Society (A.N.) and the Medical Scientist Training Program (J.L.Z.).

COMPETING INTERESTS STATEMENT

The authors declare that they have no competing financial interests.

Published online at http://www.nature.com/natureneuroscience
Reprints and permissions information is available online at http://npg.nature.com/reprintsandpermissions

1. Barbour, B. An evaluation of synapse independence. *J. Neurosci.* **21**, 7969–7984 (2001).
2. Clancy, B., Silva-Filho, M. & Friedlander, M.J. Structure and projections of white matter neurons in the postnatal rat visual cortex. *J. Comp. Neurol.* **434**, 233–252 (2001).
3. Kriegler, S. & Chiu, S.Y. Calcium signaling of glial cells along mammalian axons. *J. Neurosci.* **13**, 4229–4245 (1993).
4. Fulton, B.P., Burne, J.F. & Raff, M.C. Visualization of O-2A progenitor cells in developing and adult rat optic nerve by quisqualate-stimulated cobalt uptake. *J. Neurosci.* **12**, 4816–4833 (1992).
5. Karadottir, R., Cavelier, P., Bergersen, L.H. & Attwell, D. NMDA receptors are expressed in oligodendrocytes and activated in ischaemia. *Nature* **438**, 1162–1166 (2005).
6. Hassel, B., Boldingh, K.A., Narvesen, C., Iversen, E.G. & Skrede, K.K. Glutamate transport, glutamine synthetase and phosphate-activated glutaminase in rat CNS white matter. A quantitative study. *J. Neurochem.* **87**, 230–237 (2003).
7. Follett, P.L., Rosenberg, P.A., Volpe, J.J. & Jensen, F.E. NBQX attenuates excitotoxic injury in developing white matter. *J. Neurosci.* **20**, 9235–9241 (2000).
8. Butt, A.M. *et al.* Cells expressing the NG2 antigen contact nodes of Ranvier in adult CNS white matter. *Glia* **26**, 84–91 (1999).
9. Bergles, D.E., Roberts, J.D., Somogyi, P. & Jahr, C.E. Glutamatergic synapses on oligodendrocyte precursor cells in the hippocampus. *Nature* **405**, 187–191 (2000).
10. Lin, S.C. *et al.* Climbing fiber innervation of NG2-expressing glia in the mammalian cerebellum. *Neuron* **46**, 773–785 (2005).
11. Yang, X.W., Model, P. & Heintz, N. Homologous recombination based modification in *Escherichia coli* and germline transmission in transgenic mice of a bacterial artificial chromosome. *Nat. Biotechnol.* **15**, 859–865 (1997).
12. Lin, S.C. & Bergles, D.E. Physiological characteristics of NG2-expressing glial cells. *J. Neurocytol.* **31**, 537–549 (2002).
13. Jacobson, S. & Trojanowski, J.Q. The cells of origin of the corpus callosum in rat, cat and rhesus monkey. *Brain Res.* **74**, 149–155 (1974).
14. Aram, J.A. & Lodge, D. Validation of a neocortical slice preparation for the study of epileptiform activity. *J. Neurosci. Methods* **23**, 211–224 (1988).
15. Capogna, M., Gahwiler, B.H. & Thompson, S.M. Calcium-independent actions of alpha-latrotoxin on spontaneous and evoked synaptic transmission in the hippocampus. *J. Neurophysiol.* **76**, 3149–3158 (1996).
16. Malgaroli, A., DeCamilli, P. & Meldolesi, J. Distribution of alpha latrotoxin receptor in the rat brain by quantitative autoradiography: comparison with the nerve terminal protein, synapsin I. *Neuroscience* **32**, 393–404 (1989).
17. Hanse, E. & Gustafsson, B. Quantal variability at glutamatergic synapses in area CA1 of the rat neonatal hippocampus. *J. Physiol. (Lond.)* **531**, 467–480 (2001).
18. Bruns, D., Riedel, D., Klingauf, J. & Jahn, R. Quantal release of serotonin. *Neuron* **28**, 205–220 (2000).
19. Volterra, A. & Meldolesi, J. Astrocytes, from brain glue to communication elements: the revolution continues. *Nat. Rev. Neurosci.* **6**, 626–640 (2005).
20. Zhou, Q., Petersen, C.C. & Nicoll, R.A. Effects of reduced vesicular filling on synaptic transmission in rat hippocampal neurones. *J. Physiol. (Lond.)* **525**, 195–206 (2000).
21. Wadiche, J.I., Arriza, J.L., Amara, S.G. & Kavanaugh, M.P. Kinetics of a human glutamate transporter. *Neuron* **14**, 1019–1027 (1995).
22. Hestrin, S., Sah, P. & Nicoll, R.A. Mechanisms generating the time course of dual component excitatory synaptic currents recorded in hippocampal slices. *Neuron* **5**, 247–253 (1990).
23. Fellin, T. *et al.* Neuronal synchrony mediated by astrocytic glutamate through activation of extrasynaptic NMDA receptors. *Neuron* **43**, 729–743 (2004).
24. Young, S.H. & Poo, M.M. Spontaneous release of transmitter from growth cones of embryonic neurones. *Nature* **305**, 634–637 (1983).
25. Shen, K. & Bargmann, C.I. The immunoglobulin superfamily protein SYG-1 determines the location of specific synapses in *C. elegans*. *Cell* **112**, 619–630 (2003).
26. Huang, J.K. *et al.* Glial membranes at the node of Ranvier prevent neurite outgrowth. *Science* **310**, 1813–1817 (2005).
27. Olivares, R., Montiel, J. & Aboitiz, F. Species differences and similarities in the fine structure of the mammalian corpus callosum. *Brain Behav. Evol.* **57**, 98–105 (2001).
28. Westrum, L.E. & Blackstad, T.W. An electron microscopic study of the stratum radiatum of the rat hippocampus (regio superior, CA 1) with particular emphasis on synaptology. *J. Comp. Neurol.* **119**, 281–309 (1962).
29. Preston, R.J., Waxman, S.G. & Kocsis, J.D. Effects of 4-aminopyridine on rapidly and slowly conducting axons of rat corpus callosum. *Exp. Neurol.* **79**, 808–820 (1983).
30. Lamantia, A.S. & Rakic, P. Cytological and quantitative characteristics of four cerebral commissures in the rhesus monkey. *J. Comp. Neurol.* **291**, 520–537 (1990).
31. Stallcup, W.B. The NG2 proteoglycan: past insights and future prospects. *J. Neurocytol.* **31**, 423–435 (2002).
32. Ughrin, Y.M., Chen, Z.J. & Levine, J.M. Multiple regions of the NG2 proteoglycan inhibit neurite growth and induce growth cone collapse. *J. Neurosci.* **23**, 175–186 (2003).
33. Yang, Z. *et al.* NG2 glial cells provide a favorable substrate for growing axons. *J. Neurosci.* **26**, 3829–3839 (2006).
34. Morgenstern, D.A. *et al.* Expression and glycanation of the NG2 proteoglycan in developing, adult, and damaged peripheral nerve. *Mol. Cell. Neurosci.* **24**, 787–802 (2003).
35. Stegmuller, J., Werner, H., Nave, K.A. & Trotter, J. The proteoglycan NG2 is complexed with α-amino-3-hydroxy-5-methyl-4-isoxazolepropionic acid (AMPA) receptors by the PDZ glutamate receptor interaction protein (GRIP) in glial progenitor cells. Implications for glial-neuronal signaling. *J. Biol. Chem.* **278**, 3590–3598 (2003).
36. Iino, M. *et al.* Glia-synapse interaction through Ca^{2+}-permeable AMPA receptors in Bergmann glia. *Science* **292**, 926–929 (2001).
37. Yuan, X., Eisen, A.M., McBain, C.J. & Gallo, V. A role for glutamate and its receptors in the regulation of oligodendrocyte development in cerebellar tissue slices. *Development* **125**, 2901–2914 (1998).
38. Barres, B.A. & Raff, M.C. Proliferation of oligodendrocyte precursor cells depends on electrical activity in axons. *Nature* **361**, 258–260 (1993).
39. Bengtsson, S.L. *et al.* Extensive piano practicing has regionally specific effects on white matter development. *Nat. Neurosci.* **8**, 1148–1150 (2005).
40. Stevens, B., Porta, S., Haak, L.L., Gallo, V. & Fields, R.D. Adenosine: a neuron-glial transmitter promoting myelination in the CNS in response to action potentials. *Neuron* **36**, 855–868 (2002).
41. Dawson, M.R., Polito, A., Levine, J.M. & Reynolds, R. NG2-expressing glial progenitor cells: an abundant and widespread population of cycling cells in the adult rat CNS. *Mol. Cell. Neurosci.* **24**, 476–488 (2003).
42. Chittajallu, R., Aguirre, A. & Gallo, V. NG2-positive cells in the mouse white and grey matter display distinct physiological properties. *J. Physiol. (Lond.)* **561**, 109–122 (2004).
43. Gensert, J.M. & Goldman, J.E. Heterogeneity of cycling glial progenitors in the adult mammalian cortex and white matter. *J. Neurobiol.* **48**, 75–86 (2001).

44. McDonald, J.W., Althomsons, S.P., Hyrc, K.L., Choi, D.W. & Goldberg, M.P. Oligodendrocytes from forebrain are highly vulnerable to AMPA/kainate receptor-mediated excitotoxicity. *Nat. Med.* **4**, 291–297 (1998).
45. Rossi, D.J., Oshima, T. & Attwell, D. Glutamate release in severe brain ischaemia is mainly by reversed uptake. *Nature* **403**, 316–321 (2000).
46. Micu, I. *et al*. NMDA receptors mediate calcium accumulation in myelin during chemical ischaemia. *Nature* **439**, 988–992 (2006).
47. Jahr, C.E. High probability opening of NMDA receptor channels by L-glutamate. *Science* **255**, 470–472 (1992).
48. Tillet, E., Ruggiero, F., Nishiyama, A. & Stallcup, W.B. The membrane-spanning proteoglycan NG2 binds to collagens V and VI through the central nonglobular domain of its core protein. *J. Biol. Chem.* **272**, 10769–10776 (1997).
49. Bhat, M.A. *et al*. Axon-glia interactions and the domain organization of myelinated axons requires neurexin IV/Caspr/Paranodin. *Neuron* **30**, 369–383 (2001).
50. Fukaya, M. & Watanabe, M. Improved immunohistochemical detection of postsynaptically located PSD-95/SAP90 protein family by protease section pretreatment: a study in the adult mouse brain. *J. Comp. Neurol.* **426**, 572–586 (2000).